scientific reports

Check for updates

OPEN

# Enhanced classification of tinnitus patients using EEG microstates and deep learning techniques

Zahra Raeisi[1], Abolfazl Sodagartojgi[2], Fahimeh Sharafkhani[3], Amirsadegh Roshanzamir[4], Hossein Najafzadeh[5]✉, Omid Bashiri[6] & Alireza Golkarieh[7]

**This study aims to deepen the understanding and classification of tinnitus through a comprehensive analysis of EEG signals utilizing innovative microstate analysis techniques and cutting-edge machine learning approaches. EEG data were collected from two datasets: a primary dataset with 36 participants (16 healthy, 20 tinnitus) and a public dataset with 37 participants (15 healthy, 22 tinnitus). Signals were decomposed into five frequency bands (delta, theta, alpha, beta, gamma) using Daubechies 4 wavelet at five decomposition levels. Microstate features (Duration, Occurrence, Mean Global Field Power, and Coverage) were extracted across four microstate configurations (4-state to 7-state) under both eyes-closed and eyes-open conditions. Classification was performed using SVM, Decision Tree, Random Forest, and Deep Neural Networks. Additionally, pre-trained models (VGG16, ResNet50, Xception) were used with a novel feature-to-image transformation approach for validation. Analysis revealed significant alterations in beta band microstates, with microstate A showing increased duration (+7.8% to +11.2%) and microstate B showing decreased duration (−9.0% to −13.8%) in tinnitus patients. Occurrence rates were markedly elevated (~28–29% higher) in the tinnitus group. Transition probability analysis identified distinctive patterns between groups, with the most pronounced differences observed in gamma band (6-state configuration) during eyes-closed condition (healthy: F → B = 0.143; tinnitus: C → D = 0.153) and beta band (7-state configuration) also during eyes-closed condition (healthy: E → A = 0.091; tinnitus: C → E = 0.082). In the eyes-open condition, gamma band with 7 microstates showed substantial differences in transition patterns (healthy: E → A = 0.149; tinnitus: C → G = 0.157). Classification performance was exceptional, with DNN achieving 100% accuracy in the gamma frequency band during eyes-open condition with 5-state configuration. Frequency band analysis demonstrated that gamma band performed best for open eyes (99.89% accuracy) and beta band excelled for closed eyes (96.46% accuracy). Validation with pre-trained models showed ResNet50 with SVM classifier using 6-state configurations provided optimal discrimination (100% accuracy). EEG microstate dynamics in beta and gamma bands serve as reliable markers for distinguishing tinnitus patients. These findings provide insights into tinnitus-related neural alterations and highlight microstate analysis as a potential objective diagnostic tool for guiding personalized neuromodulation therapies.**

**Keywords** Tinnitus, EEG microstates, Deep learning, Classification

The human auditory system enables sound perception essential for communication and environmental interaction by converting sound waves into neural impulses. It comprises the outer, middle, and inner ear, with the cochlea transforming mechanical waves into electrical signals sent to the brain via the auditory nerve[1,2]. Damage to any of these structures can result in hearing impairments[3]. Tinnitus, affecting 10–15% of the population, manifests as persistent sounds like ringing or buzzing, significantly impacting the quality of life in

[1]Department of Computer Science, University of Fairleigh Dickinson, Vancouver Campus, Vancouver, Canada. [2]Department of Statistics, Rutgers University, New Brunswick, NJ, USA. [3]Engineering Management and Systems Engineering Department, Missouri University of Science and Technology, Rolla, MO 65401, USA. [4]Department of Information Systems and Management, University of South Florida, Tampa, FL, USA. [5]Department of Medical Bioengineering, Faculty of Advanced Medical Sciences, Tabriz University of Medical Sciences, Golgasht Ave, Tabriz 51666, Iran. [6]Department of Kinesiology and Nutrition Sciences, University of Nevada, Las Vegas, Las Vegas, NV 89154, USA. [7]PhD Student in Computer Science and Informatics, Department of Computer Science and Engineering, Oakland University, Rochester, MI, USA. ✉email: najafzadeh@tbzmed.ac.ir

1–2% of individuals[4]. This condition is associated with prolonged noise exposure, aging, ototoxic medications, or head injuries and is linked to neurophysiological changes in auditory and non-auditory pathways involved in attention and emotional regulation[5,6]. Tinnitus also causes secondary effects such as sleep disturbances, anxiety, and depression, further affecting well-being[7,8]. While existing treatments like cognitive-behavioral therapy and sound therapy provide symptomatic relief, their effectiveness is limited due to the complex and diverse causes of tinnitus[9]. The rising prevalence and severe impacts of tinnitus underscore the need for innovative therapies targeting both its auditory and emotional dimensions.

Bimodal neuromodulation, which combines auditory and somatosensory stimulation, shows promise in alleviating tinnitus symptoms. Shore et al. demonstrated its effectiveness in modulating dorsal cochlear nucleus activity, reducing tinnitus in animal models[10]. A clinical trial with 326 participants reported lasting improvements in tinnitus severity scores for up to 12 months[11], and devices like the Neosensory Duo further support its potential for non-invasive treatment[12]. However, the lack of objective assessment methods limits broader clinical application. Advanced tools like EEG, fMRI, and fNIRS can aid in understanding neural changes, with EEG being particularly advantageous due to its high temporal resolution, affordability, and portability[13–15].

Recent studies suggest that subjective tinnitus is associated with irregular firing patterns in central neurons, which can be effectively analyzed using EEG microstate analysis. This method captures rapid shifts in brain states with high temporal resolution, providing insights into neural dynamics related to cognition and behavior[16,17]. Research on tinnitus patients has identified distinctive patterns in EEG microstates, such as altered transitions between Microstates D and B, reduced amplitude and occurrence of Microstate A, and increased activity in Microstate B, particularly in patients with sudden sensorineural hearing loss (SSNHL)[18,19]. Other studies report increased engagement of Microstate C, associated with regions like the left middle temporal gyrus, linked to sound detection and suppression, while differences in the duration of Microstates A, C, and D have been correlated with tinnitus severity[20,21]. Additionally, microstate alterations in patients with vestibular schwannoma (VS) and tinnitus reveal correlations between tinnitus severity and changes in Microstates A and C, highlighting their potential role in symptom manifestation[22].

Recent advancements in machine learning and deep learning have provided new approaches to classifying tinnitus patients using EEG data, addressing the limitations of traditional diagnostic methods. Sun introduced a multi-view intact space learning method that segmented EEG data to improve classification performance despite a limited dataset, achieving over 98% accuracy, recall, precision, and F1 scores using an SVM classifier[23]. Similarly, Zhou extracted specific EEG frequency components to analyze tinnitus-related patterns through deep neural networks (DNN), achieving a 92% classification accuracy. These studies highlight the potential of feature extraction and model optimization in distinguishing tinnitus from non-tinnitus EEG profiles effectively[24]. Building on this foundation, recent studies by Hong and Jianbiao focused on identifying specific EEG markers for tinnitus. Hong's analysis, using EEGNet during oddball tasks, revealed reduced alpha and theta activities in tinnitus patients, suggesting these features as neural signatures. Jianbiao further identified heightened entropy values in certain EEG frequency bands, indicating distinct neural chaos associated with tinnitus, and achieved a classification accuracy of 91.38% using an SVM[25]. Doborjeh's study advanced this work by predicting therapy responses in tinnitus patients with up to 100% accuracy using AI models on EEG data, suggesting a path toward personalized treatment strategies. Furthermore, the intricate nature and individual variability of tinnitus create substantial challenges for neurobiological research and objective diagnosis[26]. In this context, the combined insights from various studies highlight the potential of EEG-based machine learning models not only for diagnosing tinnitus but also for predicting treatment responses. This presents an encouraging advancement for both clinicians and researchers in the field.

Analyzing EEG microstates during eyes-closed resting-state conditions offers valuable insights into neural patterns unique to tinnitus patients compared to healthy controls. The absence of visual stimuli during eyes-closed states modulates neural dynamics, reorienting sensory processing networks and amplifying internal auditory activity, which may reveal distinct microstate characteristics in tinnitus[27,28]. Parameters such as the stability and frequency of specific microstates can highlight sensory-related abnormalities and irregularities in resting-state brain activity in tinnitus patients[29,30]. Additionally, comparing microstates across eyes-open and eyes-closed conditions may identify tinnitus-specific markers linked to auditory and multimodal integration dysfunctions[31]. This approach holds promise for uncovering objective biomarkers, enhancing understanding of tinnitus's neurophysiological mechanisms, and improving diagnostic accuracy.

Prior studies on tinnitus have made substantial advances in understanding its neurophysiological underpinnings; however, challenges remain in identifying objective markers specific to this condition, particularly due to individual variability and complex neural dynamics. Conventional EEG analyses often overlook nuanced temporal changes in brain networks, limiting their ability to capture subtle yet critical differences in tinnitus-related neural activity. Additionally, most existing research focuses on single-state analyses or limited frequency bands, missing potentially relevant data across microstate configurations and frequency spectrums. This study aims to address these gaps by utilizing EEG microstate analysis across four distinct configurations (4-state, 5-state, 6-state, and 7-state) in both tinnitus and control groups. We compare EEG microstate parameters, including Duration, Occurrence, Coverage, and mean GFP, across delta, theta, alpha, beta, and gamma bands, seeking to identify markers specific to chronic subjective tinnitus. Furthermore, our study integrates these features into machine learning and transfer learning models, facilitating accurate classification between tinnitus and control subjects. By examining the correlations between EEG microstate parameters and subjective tinnitus characteristics, this study offers an innovative approach to identifying objective neurophysiological markers and proposes potential frameworks for more precise tinnitus diagnostics.

## Materials and methods

### EEG dataset

*Participants in this study were divided into two groups*

The study included two groups: a tinnitus group and a control group, both carefully selected to ensure comparability and control for potential confounding factors. The tinnitus group consisted of 20 participants (12 women and 8 men; mean age = 47.2 years, SD = 14.8) who experienced chronic tinnitus for durations ranging from one to thirty years. To minimize external influences, none of these participants had taken any medication within two weeks prior to the study. Exclusion criteria for this group included neurological disorders, active ear infections, and significant hearing loss unrelated to tinnitus. Participants were recruited from the Iran Rehabilitation Institute and local clinics, and each underwent thorough medical history evaluations and physical examinations to verify eligibility. Table 1 provides a detailed summary of the tinnitus-related parameters and audiological assessments for each participant in the tinnitus group. It includes information on the laterality of tinnitus (left or right ear), pitch (frequency in Hertz), and loudness (intensity in decibels). Additionally, hearing loss was measured both in decibels and through an indexed value, giving a comprehensive view of auditory health. Psychological assessments yielded scores for anxiety and depression, while tinnitus severity was evaluated using the Tinnitus Handicap Inventory (THI), reflecting the overall impact of tinnitus on each participant's quality of life. The control group consisted of 16 healthy individuals (8 women and 8 men; mean age = 31.1 years, SD = 10.2) with no history of tinnitus or other significant medical conditions. Exclusion criteria mirrored those of the tinnitus group, excluding any history of neurological disorders, ear infections, or hearing impairments. These participants were recruited from the general population and underwent identical screening processes to confirm eligibility, ensuring comparability between groups.The Ethics Committee approved the study's methodology, with trial registration number ISRCTN14553550, certifying that all participants met stringent inclusion criteria[32]. This rigorous approach provides a reliable foundation for analyzing the characteristics and impacts of tinnitus.

*Ethics statement*

All methods were carried out in accordance with relevant guidelines and regulations. Informed consent was obtained from all subjects and/or their legal guardian(s) prior to participation in the study. The Ethics Committee of Tabriz University of Medical Sciences, Tabriz, Iran, approved the study's methodology, with trial registration number ISRCTN14553550, certifying that all participants met stringent inclusion criteria.

*EEG recordings*

EEG data for both groups were collected using a 64-channel system while participants rested under two conditions: eyes closed and eyes open. Each recording session lasted 10 min, with the first 5 min conducted with eyes closed followed by 5 min with eyes open. Electrodes were positioned according to the international 10–10 system, with Cz as the reference channel and the left earlobe as the ground. Each participant was seated comfortably in a quiet, dimly lit room and instructed to relax and minimize cognitive activity. EEG signals were recorded at a sampling rate of 1200 Hz, ensuring high temporal resolution, while electrode impedance was maintained below 50 kΩ to optimize signal quality. The EEG electrodes were connected to an amplifier via a

| Participant | Sex | Side | Pitch (Hz) | Loudness (dB) | Hearing Loss (Decibel) | Hearing Loss (Index) | Anxiety Score | Depression Score | Tinnitus Severity |
|---|---|---|---|---|---|---|---|---|---|
| P1 | Female | Left | 6000 | 30 | 11 | 16 | 1 | 1 | 3 |
| P2 | Female | Left | 8000 | 50 | 22 | 26 | 1 | 1 | 3 |
| P3 | Male | Left | 10,000 | 50 | 11 | 18 | 1 | 1 | 2 |
| P4 | Male | Right | 1500 | 15 | 6 | 8 | 2 | 1 | 2 |
| P5 | Female | Right | 8000 | 15 | 18 | 21 | 1 | 1 | 2 |
| P6 | Female | Left | 11,200 | 90 | 8 | 12 | 1 | 1 | 3 |
| P7 | Male | Right | 2000 | 35 | 18 | 16 | 1 | 1 | 2 |
| P8 | Female | Right | 8000 | 20 | 41 | 46 | 1 | 1 | 3 |
| P9 | Female | Right | 6000 | 10 | 15 | 16 | 1 | 1 | 3 |
| P10 | Male | Right | 4000 | 10 | 20 | 19 | 3 | 2 | 2 |
| P11 | Female | Left | 9000 | 40 | 17 | 24 | 2 | 2 | 3 |
| P12 | Male | Left | 3000 | 25 | 13 | 14 | 1 | 1 | 1 |
| P13 | Female | Right | 5000 | 45 | 20 | 25 | 1 | 1 | 2 |
| P14 | Male | Right | 2500 | 30 | 12 | 10 | 2 | 1 | 2 |
| P15 | Female | Left | 7000 | 50 | 14 | 18 | 1 | 1 | 3 |
| P16 | Female | Right | 10,000 | 55 | 21 | 30 | - | - | - |
| P17 | Male | Left | 2000 | 20 | 19 | 21 | - | - | - |
| P18 | Female | Right | 6000 | 35 | 16 | 20 | 2 | 1 | 3 |
| P19 | Male | Left | 4000 | 15 | 12 | 15 | 1 | 1 | 2 |
| P20 | Female | Left | 7500 | 25 | 18 | 22 | 1 | 2 | 2 |

**Table 1**. Characteristics and audiological assessments of tinnitus group participants.

GAMMAbox, ensuring stable signal acquisition. This setup allowed for a comprehensive assessment of neural activity across both resting-state conditions. Figure 1 illustrates the 64-channel EEG electrode placement based on the 10–10 system, covering key brain regions for extensive neural data acquisition.

## Publicly available EEG dataset for tinnitus and healthy controls

A publicly accessible EEG dataset is available for tinnitus research, containing recordings from two distinct groups: 15 healthy individuals as a control group and 22 individuals diagnosed with tinnitus. EEG signals were recorded under an eyes-open condition with a sampling rate of 256 Hz for 2 min. The data were collected using 19 electrodes positioned according to the international 10–20 system, ensuring consistency in electrode placement. Table 2 summarizes the audiological characteristics of the tinnitus participants, including their average hearing levels, tinnitus classification, predominant tinnitus frequency, perceived intensity, and psychological assessment scores.

## Preprocessing steps

In this study, a series of preprocessing steps was applied to enhance data quality and optimize EEG signals for subsequent analysis. The steps are as follows.

*Data segmentation and filtering*

EEG data from both tinnitus and control groups were segmented into 1-s epochs (1200 samples per epoch, given the 1200 Hz sampling rate). A 3rd-order Butterworth bandpass filter (0.5–50 Hz) was applied to each segment, effectively removing artifacts while preserving essential signal components. This filter is commonly used in EEG research due to its ability to minimize noise without distorting the signal[33].

*Data normand correction*

Each EEG segment was normalized using z-score normalization, ensuring a mean of zero and a standard deviation of one for consistency across all samples. Additionally, the mean of each normalized segment was subtracted to correct for DC offset and eliminate low-frequency noise. The normalized value $x_{norm}$ for each segment x was computed as[34]:

$$x_{norm} = \frac{x - \mu}{\sigma} \tag{1}$$

where $\mu$ is the mean and $\sigma$ is the standard deviation of $x$.

*Signal decomposition using wavelet transform*

The EEG signals were decomposed into five frequency bands: delta (0.5–4 Hz), theta (5–8 Hz), alpha (9–13 Hz), beta (14–30 Hz), and gamma (31–50 Hz) using wavelet transform. The wavelet transform is a powerful tool for time–frequency analysis, enabling precise localization of signals across different frequency ranges. The mother wavelet, Daubechies 4 (db4), was selected due to its suitability for EEG signal processing, preserving both time and frequency information.

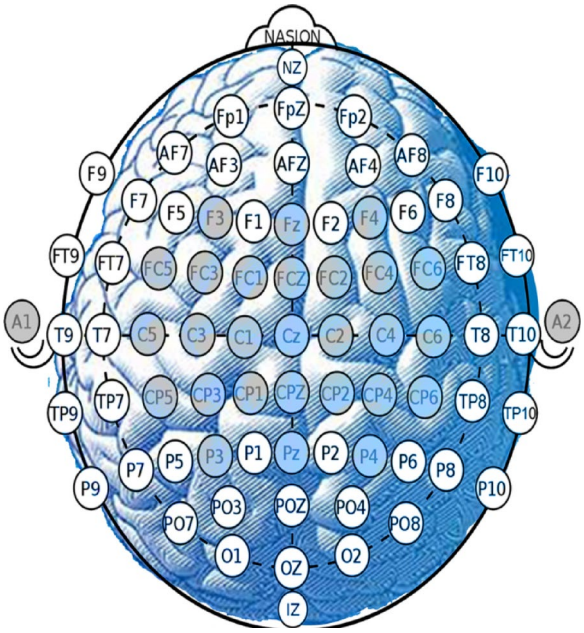


**Fig. 1**. Electrode placement map for 64-channel EEG cap.

| Participant ID | Average hearing threshold (dB HL) | Tinnitus type | Predominant frequency (Hz) | Perceived loudness (dB HL) | Anxiety score | Depression score | TFI index |
|---|---|---|---|---|---|---|---|
| T1 | 32 | Mixed | 8 | 55 | 16 | 11 | 69.2 |
| T2 | 23 | Mixed | 8 | 85 | 5 | 5 | 28.8 |
| T3 | 47.25 | Tonal | 8 | 70 | 14 | 9 | 62.8 |
| T4 | 11 | Tonal | 2 | 60 | 13 | 7 | 60.4 |
| T5 | 25.25 | Mixed | 1.5 | 35 | 7 | 7 | 48 |
| T6 | 21.25 | Mixed | 8 | 65 | 10 | 8 | 50.8 |
| T7 | 32 | Mixed | 4 | 55 | 12 | 11 | 64.4 |
| T8 | 28.75 | Mixed | 6 | 52 | 8 | 2 | 45.6 |
| T9 | 7 | Mixed | 4 | 15 | 7 | 3 | 54.8 |
| T10 | 26.75 | Mixed | 10 | 45 | 12 | 4 | 44.4 |
| T11 | 16 | Mixed | 8 | 55 | 4 | 1 | 18.4 |
| T12 | 26.25 | Tonal | 8 | 45 | 2 | 1 | 23.2 |
| T13 | 20.5 | Tonal | 8 | 47 | 6 | 4 | 51.6 |
| T14 | 3 | Mixed | 3.5 | 25 | 7 | 4 | 77.2 |
| T15 | 10.75 | Tonal | 10 | 45 | 7 | 6 | 26.4 |
| T16 | 32.75 | Mixed | 6 | 47 | 18 | 8 | 60.4 |
| T17 | 36.5 | Mixed | 3 | 55 | 14 | 8 | 67.6 |
| T18 | 81.25 | Mixed | 10 | 115 | 4 | 2 | 38.4 |
| T19 | 14 | Tonal | 6 | 25 | 4 | 5 | 32 |
| T20 | 13.5 | Tonal | 3 | 45 | 9 | 12 | 57.6 |
| T21 | 26.25 | Mixed | 2 | 30 | 16 | 11 | 49.5 |
| T22 | 14 | Mixed | 6 | 35 | 18 | 4 | 67.4 |

**Table 2**. Audiometric and psychological profiles of tinnitus participants.

Each EEG signal was decomposed into approximation and detail coefficients at five decomposition levels (level 5) using discrete wavelet transform (DWT). The selection of level 5 decomposition was based on the need to accurately separate EEG sub-bands while maintaining computational efficiency. The frequency bands were extracted based on the following relationship[35]:

$$f_j = \frac{f_s}{2^{j+1}} \;\; to \;\; \frac{f_s}{2^j} \tag{2}$$

where $f_j$ is the frequency range at decomposition level $j$ and $f_s$ is the sampling frequency. These coefficients were then used to reconstruct the respective frequency bands for further analysis. Figure 2 presents EEG signals from healthy and tinnitus subjects. The first two rows show raw and preprocessed signals, while the following rows depict wavelet-extracted frequency sub-bands. This analysis highlights spectral differences between the two groups.

## Extraction of features from EEG data for microstate analysis

In this study, K-means clustering was employed to categorize EEG data into distinct microstate classes, structured across four configurations: 4-state (A, B, C, D), 5-state (A, B, C, D, E), 6-state (A, B, C, D, E, F), and 7-state (A, B, C, D, E, F, G). Key features extracted for each microstate class included Duration, Occurrence per second, Coverage, Global Field Power (GFP), Transition Probabilities, and Frequency. These features offer insights into the temporal and spatial dynamics of brain activity. Below, each feature is defined, along with the formulas used to calculate them.

*Duration*

The Duration of a microstate class represents the time span, in milliseconds, that a particular microstate remains active. This is calculated as follows:

$$Duration_{class} = t_{end} - t_{start} \tag{3}$$

where $t_{start}$ represents the start time of the microstate class and $t_{end}$ denotes the end time of the microstate class[36], The mean duration across all microstate classes is:

$$Mean\ Duration_{All} = \frac{\sum_{i=1}^{N} Duration_{class_i}}{N} \tag{4}$$

where N is the total number of microstate classes, which could vary between 4, 5, 6, or 7 depending on the configuration[37].

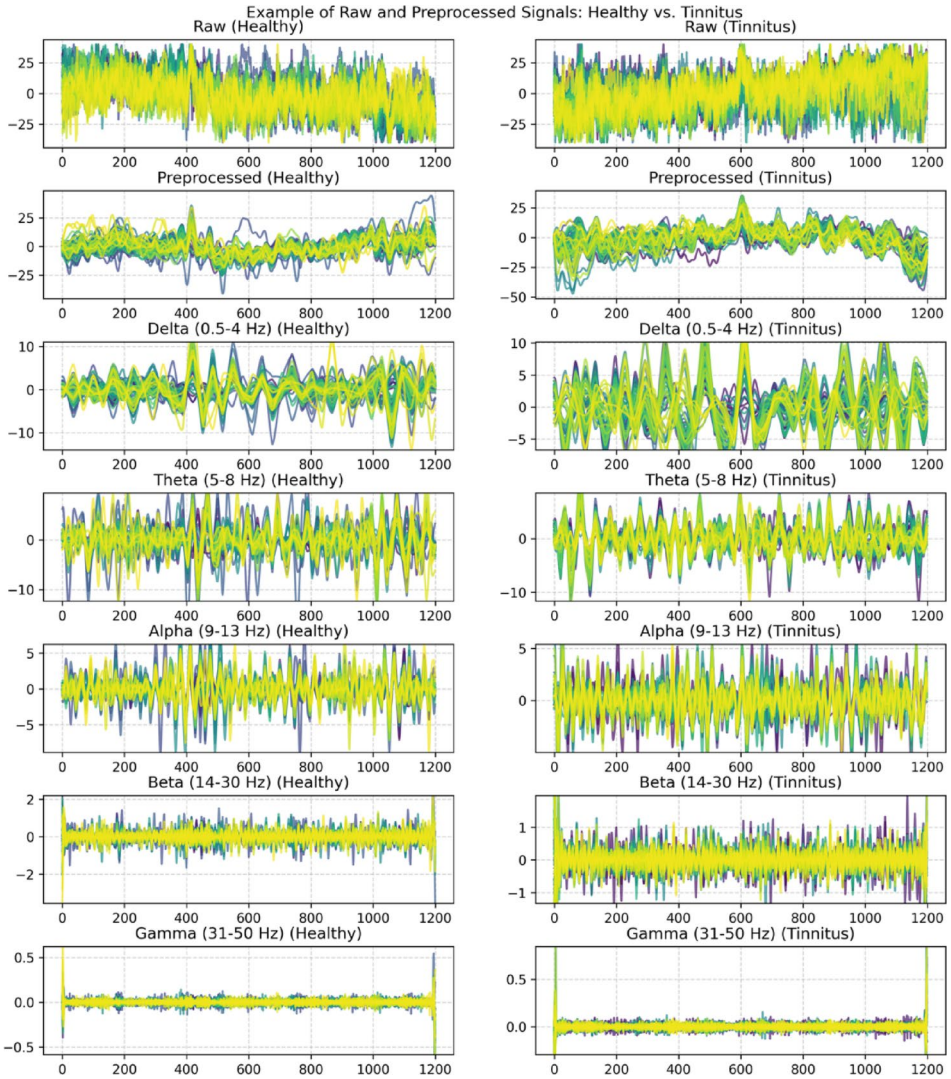


**Fig. 2**. An example of comparison of overlaid EEG signals and frequency sub-bands in healthy and tinnitus subjects (1-second segment).

*Occurrence per second*
This metric describes how frequently a microstate class appears per second during the analysis period:

$$Occurrence/s_{class} = \frac{Total\ Occurrences\ of\ Class}{Total\ Analysis\ Time\ in\ Seconds} \tag{5}$$

where Total Occurrences refers to the number of times a specific microstate class is observed, and Total Analysis Time represents the overall duration of the analysis in seconds[38].

*Coverage*
Coverage refers to the percentage of the total analysis time that each microstate class occupies, expressed as a proportion:

$$Coverage_{class} = \left(\frac{\sum Duration_{class}}{Total\ Analysis\ Time}\right) \times 100 \tag{6}$$

This metric indicates the extent of time each class dominates within the entire analysis duration, providing insight into the predominant patterns in brain activity[38].

*Global field power (GFP)*
Represents the instantaneous field power across the brain, calculated as:

$$GFP = \sqrt{\left(\sum_{i}^{k}(V_i(t) - V_{mean}(t)\right)^2 /k} \tag{7}$$

where $V_i\,(t)$ represents the signal from each channel at time *t*, $V_{mean}\,(t)$ indicates the mean signal across channels at time t, and *k* denotes the total number of channels[39].

This calculation of GFP quantifies the signal's spatial variance, capturing the momentary strength of the global electric field.

*Transition probabilities*

The transition probability metric quantifies the likelihood of shifting from one microstate class to another, offering insight into sequential brain dynamics[40]:

$$P_{ij} = \frac{Transitions\ from\ i\ to\ j}{Totla\ transitions\ from\ i} \tag{8}$$

where $P_{ij}$ denotes the probability of transitioning from microstate $i$ to microstate $j$.

Figure 3 shows an example of extracting 4-state, 5-state, 6-state, and 7-state microstates from a 64-channel EEG signal over a 4-s duration. A 1-s sliding window is applied to calculate the Global Field Power (GFP), and the k-means clustering method is used to identify the microstates (A–G). The topographical maps represent the distinct spatial patterns of brain activity for each microstate configuration.

*Feature-to-image transformation*

In this study, microstate-based features including Duration, Occurrence, Mean Global Field Power (GFP), and Coverage were extracted from each 1-s EEG segment recorded from both healthy individuals and tinnitus patients. These features were then transformed into 20 × 20 grayscale images based on microstate configurations across the delta, theta, alpha, beta, and gamma frequency bands. In each image, rows represent temporal EEG windows,

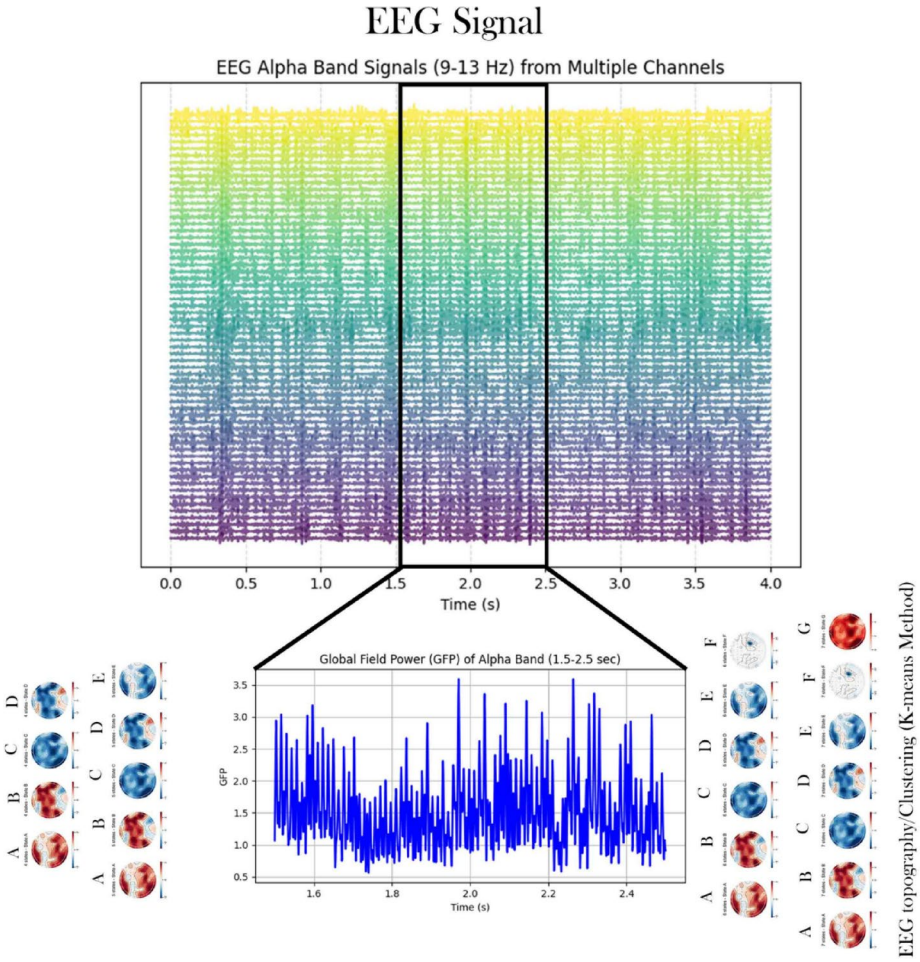


**Fig. 3**. Sample of EEG signal in the alpha band, topographic clustering, and global field power (GFP).

while columns correspond to specific features within different frequency bands and microstate categories. All pixel intensities were normalized to a [0, 1] range to ensure consistent representation. This transformation aimed to convert non-image EEG features into a structured format suitable for 2D convolutional neural networks (CNNs), facilitating the automated learning of temporal and cross-feature patterns. Unlike prior approaches that focused on spatial effective connectivity matrices (e.g., $32\times32$ or $19\times19$ adjacency representations based on EEG channels[41,42]), the proposed method generates $20\times20$ matrices where each pixel reflects the temporal progression of a given feature across time, frequency, and microstate configuration dimensions. This design preserves the temporal dynamics of brain microstates and enables CNNs to capture subtle yet informative temporal variations between clinical and non-clinical populations. The resulting image-based representations serve as a bridge between sequential EEG features and spatial deep learning models. The overall transformation process is depicted in Fig. 4.

## Model development

*DNN structure*

The Deep Neural Network (DNN) implemented in this study is designed for binary classification and consists of an input layer, three hidden layers, and an output layer. The hidden layers include 64, 32, and 16 neurons, respectively, with each layer using Rectified Linear Unit (ReLU) activation, a function known for effectively addressing the vanishing gradient problem and improving network depth[43]. Dropout regularization is applied to the hidden layers, helping to reduce overfitting by randomly omitting a fraction of neurons during training[44]. Additionally, batch normalization is employed to improve training stability and convergence, enabling the model to reach optimal performance more efficiently[45]. The output layer consists of two neurons with a sigmoid activation function for binary classification, converting the model's output to a probability score between 0 and 1. The Adam optimizer, known for its adaptive learning rates and computational efficiency, is employed in this architecture, making it particularly suitable for handling large datasets[46]. The model uses binary cross-entropy loss, which is standard for binary classification tasks. With specific learning parameters as detailed in Table 3, this DNN configuration is designed to deliver consistent and robust classification outcomes. Figure 5 illustrates the DNN architecture designed for classifying EEG microstate features.

*Pre-trained Models: VGG16, ResNet50, and Xception*

We evaluated the classification performance of three pre-trained models: VGG16, ResNet50, and Xception, using features transformed into grayscale images. To meet the models' three-channel RGB input requirements, the single-channel images were duplicated. Microstate features from five frequency bands (delta, theta, alpha, beta, gamma) were combined to generate 15 images of $20\times20$ pixels for each microstate. These images were resized to $224\times224$ pixels with zero-padding to ensure compatibility with the pre-trained models.

Fine-tuning VGG16 VGG16 is a Convolutional Neural Network (CNN) architecture consisting of 16 layers, known for its simplicity and effectiveness in image classification tasks. It utilizes small $3\times3$ filters across all convolutional layers and ends with fully connected layers for classification. Mathematically, the operation in each convolutional layer of VGG16 can be expressed as follows[47]:

$$Z_{l+1} = f\left(W_l * Z_l + b_l\right) \tag{9}$$

where $Z_{l+1}$ represents the output of layer $l+1$, $W_l$ denotes the weights in layer , * signifies the convolution operation, $b_l$ is the bias term, and $f$ is the activation function, which is ReLU in the case of VGG16. Figure 6 illustrates the process of converting feature matrices into $224\times224$ RGB images, passing them through VGG16 layers, and classifying the extracted features using SVM, Decision Tree (DT), and Random Forest (RF). Pre-trained on ImageNet, the VGG16 model is customized for this classification task, as shown in Table 3 with specific learning parameters and optimizer configurations.

## Fine-tuning ResNet50

ResNet50 is a deep CNN architecture with 50 layers, designed to address the vanishing gradient problem through residual learning. By introducing residual blocks, ResNet50 allows the model to learn residual functions with respect to layer inputs, thereby enhancing performance in deep networks. The core operation in ResNet50 is represented by the residual block as follows[48]:

$$Z_{l+1} = f\left(Z_l + F(Z_l, W_l)\right) \tag{10}$$

where $F$ denotes the residual function, $Z_l$ is the input to the -th residual block, $W_l$ represents the weights of the -th layer, and $f$ is the activation function. Figure 7 outlines the conversion of feature matrices to $224\times224$ RGB images, processing through ResNet50, and classifying features with SVM, Decision Tree (DT), and Random Forest (RF). Fine-tuned with ImageNet weights, ResNet50 is adapted for binary classification in this study. Table 3 lists all relevant parameters, including optimizer settings and learning rate.

*Fine-tuning Xception*

The Xception (Extreme Inception) architecture is an extension of the traditional Inception model, designed for improved efficiency and performance. Instead of standard Inception modules, Xception utilizes depthwise separable convolutions, which decompose the convolution operation into two distinct steps: depthwise and pointwise convolutions. This approach reduces computational cost while enhancing the model's ability to capture intricate patterns in the data.

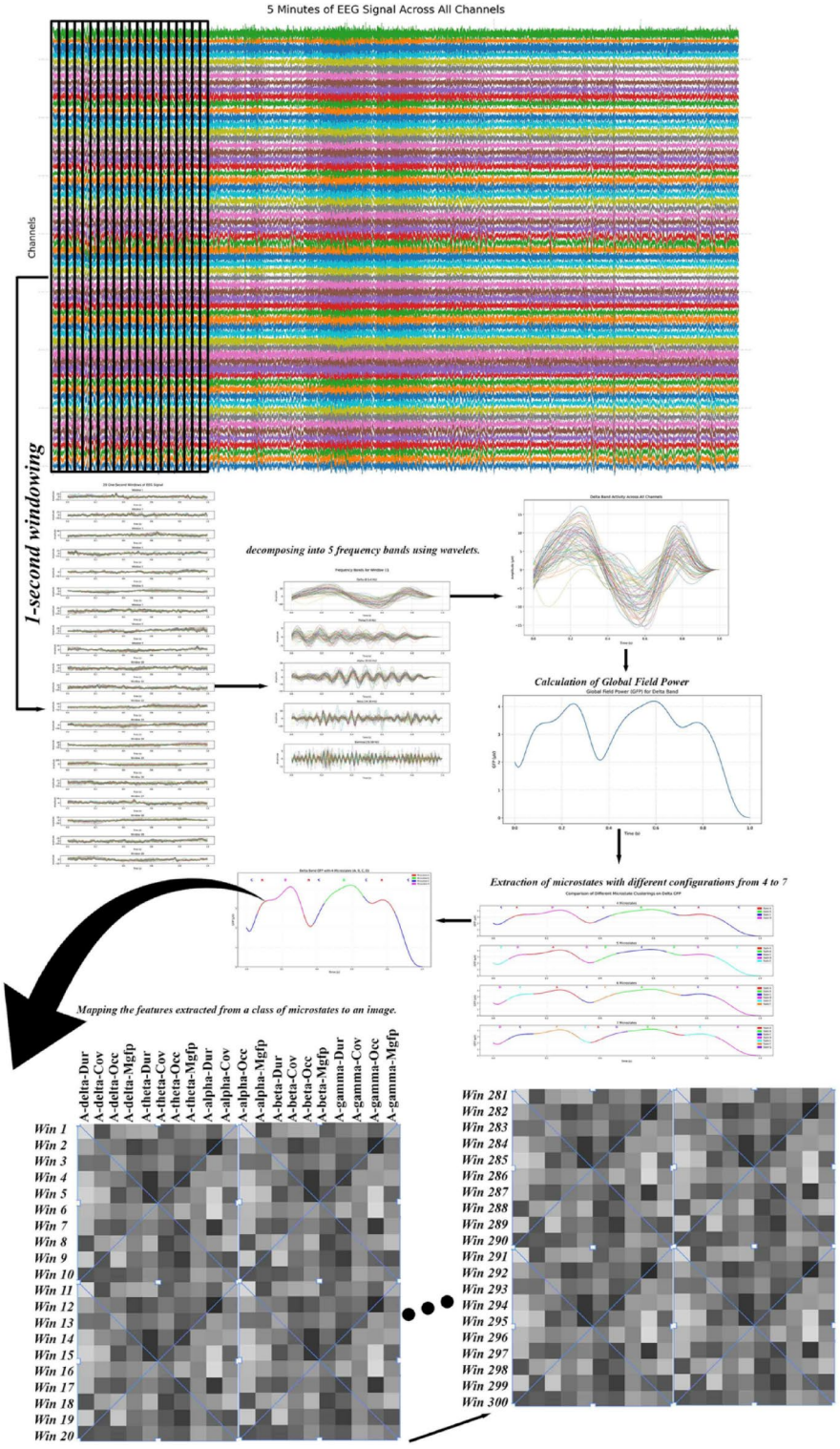


**Fig. 4**. Feature-to-image transformation pipeline: mapping extracted EEG microstate features into a two-dimensional image representation.

The depthwise separable convolution operation in Xception can be mathematically represented as[49]:

$$Z_{l+1} = f\left(W_l^d *_d (W_l^p *_p Z_l) + b_l\right) \tag{11}$$

where $*_d$ denotes the depthwise convolution, $*_p$ denotes the pointwise convolution, $W_l^d$ and $W_l^p$ represent the weights for the depthwise and pointwise convolutions, respectively, and $f$ is the activation function. Figure 8

| Model | Architecture details | Learning parameters | Cross-validation (K-fold = 5) | Activation function |
|---|---|---|---|---|
| DNN | Input: N-features, Hidden layers: [64, 32, 16 neurons], Output: 1 neuron | Optimizer: Adam, Loss: Binary Cross-Entropy, Batch Size: 32, Epochs: 50, Dropout: 0.5, Batch Norm: True, Kernel Regularization: l1 = 0.005, l2 = 0.001 | Yes | ReLU (hidden), Sigmoid (output) |
| SVM | – | Standardize Data: True, Solver: SMO, Cross-Validation: 5, Kernel: RBF, C: 1.0, Gamma: 'scale', probability = True | Yes | Tanh |
| DT | – | Standardize Data: True, Criterion: 'gini', Max Depth: None, Min Samples Split: 2 | Yes | |
| RF | – | Standardize Data: True, Number of Estimators: 100, Criterion: 'gini', Max Features: 'auto' | Yes | |
| ResNet50 | Input Layer: ImageNet weights, GlobalAveragePooling2D, Dense: 1024 | Optimizer: Adam, Learning Rate: 0.0001, Early Stopping Patience: 5, Batch Size: 8, Epochs: 50 | Yes | ReLU (hidden), Sigmoid (output) |
| Xception | Input Layer: ImageNet weights, GlobalAveragePooling2D, Dense: 1024 | Optimizer: Adam, Learning Rate: 0.0001, Early Stopping Patience: 5, Batch Size: 8, Epochs: 50 | Yes | ReLU (hidden), Sigmoid (output) |
| VGG16 | Input Layer: ImageNet weights, GlobalAveragePooling2D, Dense: 1024 | Optimizer: Adam, Learning Rate: 0.0001, Early Stopping Patience: 5, Batch Size: 8, Epochs: 50 | Yes | ReLU (hidden), Sigmoid (output) |

**Table 3**. Model architectures and training parameters.

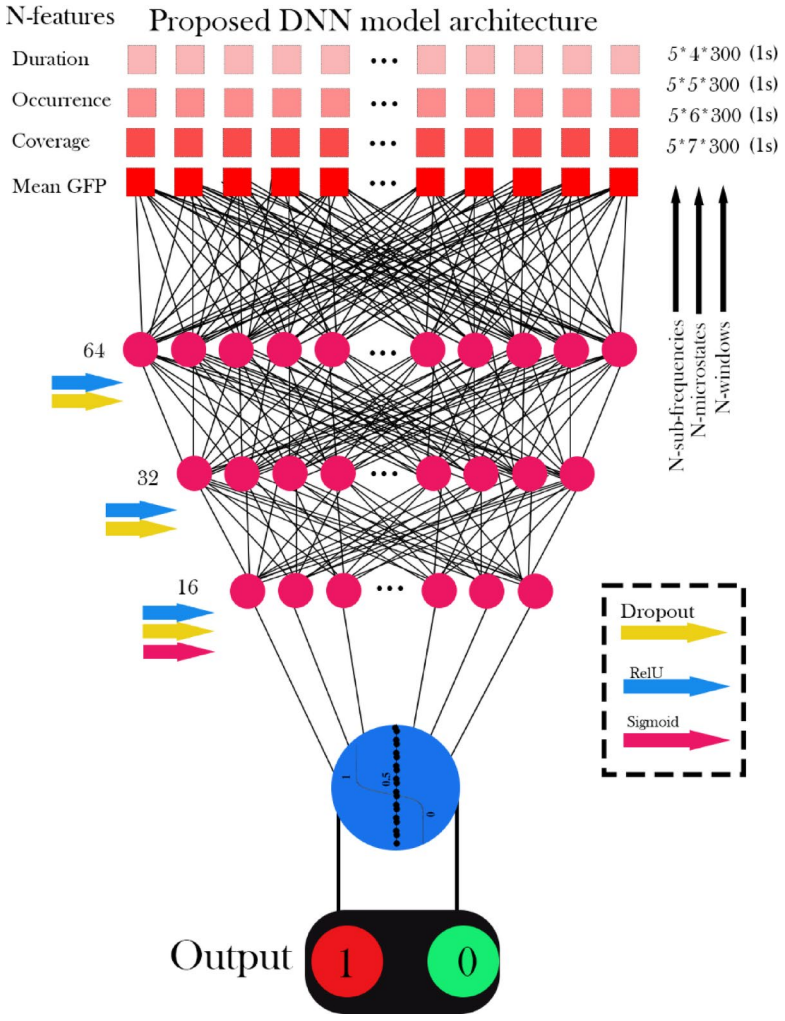


**Fig. 5**. Proposed deep neural network (DNN) model architecture for eeg microstate feature classification.

illustrates how the 20 × 20 feature matrix is converted into a 224 × 224 RGB image, processed through the Xception model, and subsequently classified using SVM, DT, and RF classifiers. The Xception model, initialized with ImageNet weights, is fine-tuned for efficient feature extraction. Detailed training parameters are presented in Table 3.

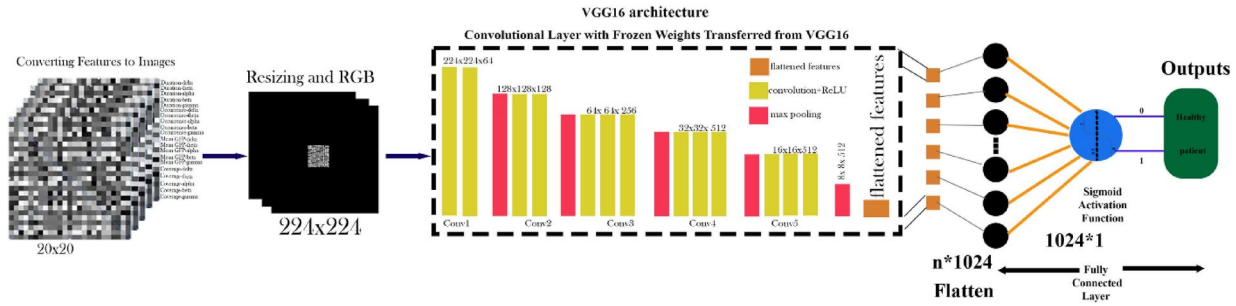


**Fig. 6**. Overview of EEG feature matrix classification using VGG16 architecture and traditional classifiers.

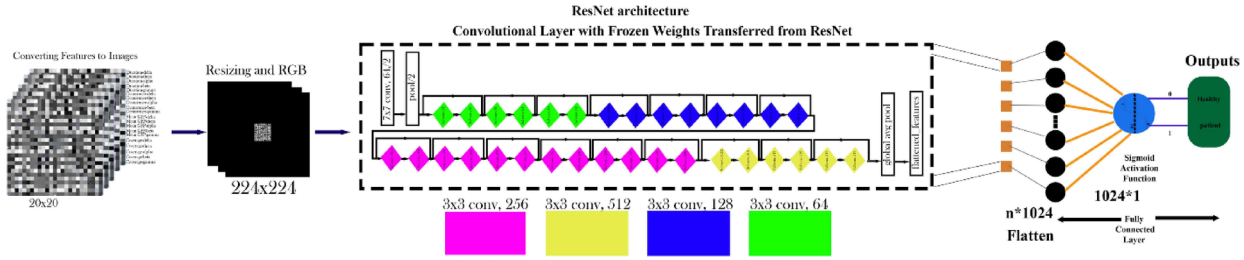


**Fig. 7**. Overview of EEG feature matrix classification using ResNet architecture and traditional classifiers.

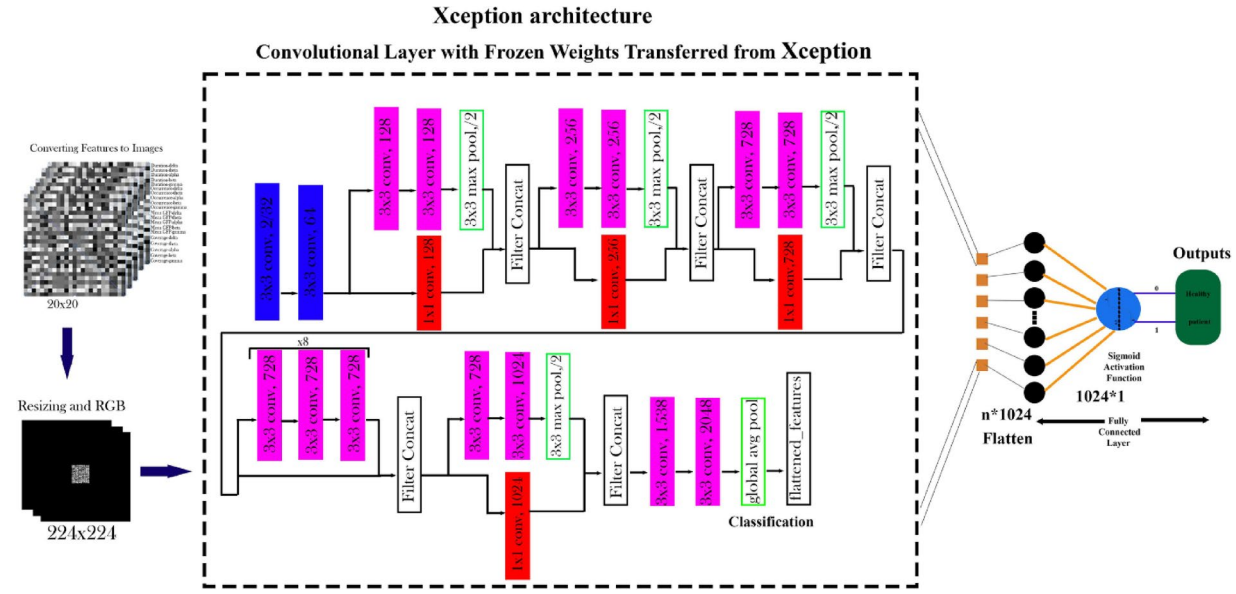


**Fig. 8**. Overview of EEG feature matrix classification using Xception architecture and traditional classifiers.

*Hybrid models: pre-trained models with SVM, RF, and DT*

Hybrid models were developed by combining pre-trained models (VGG16, ResNet50, Xception) with traditional classifiers, including SVM, RF, and DT, to enhance classification performance. The pre-trained models were used for feature extraction, while SVM, RF, and DT handled the classification[50–52]. The SVM employed an RBF kernel, with hyperparameters optimized for better results. The RF model utilized 100 decision trees to form a robust ensemble classifier, and the DT model applied the "gini" criterion for node splitting to improve generalization. Detailed learning parameters and configurations are provided in Table 3.

Figure 9 illustrates the proposed methodology for EEG signal classification, including preprocessing, microstate analysis, feature extraction, and classification using hybrid models and pre-trained models. The diagram outlines the integration of pre-trained models (VGG16, ResNet50, Xception) and machine learning classifiers (SVM, RF, DT) for optimized performance.

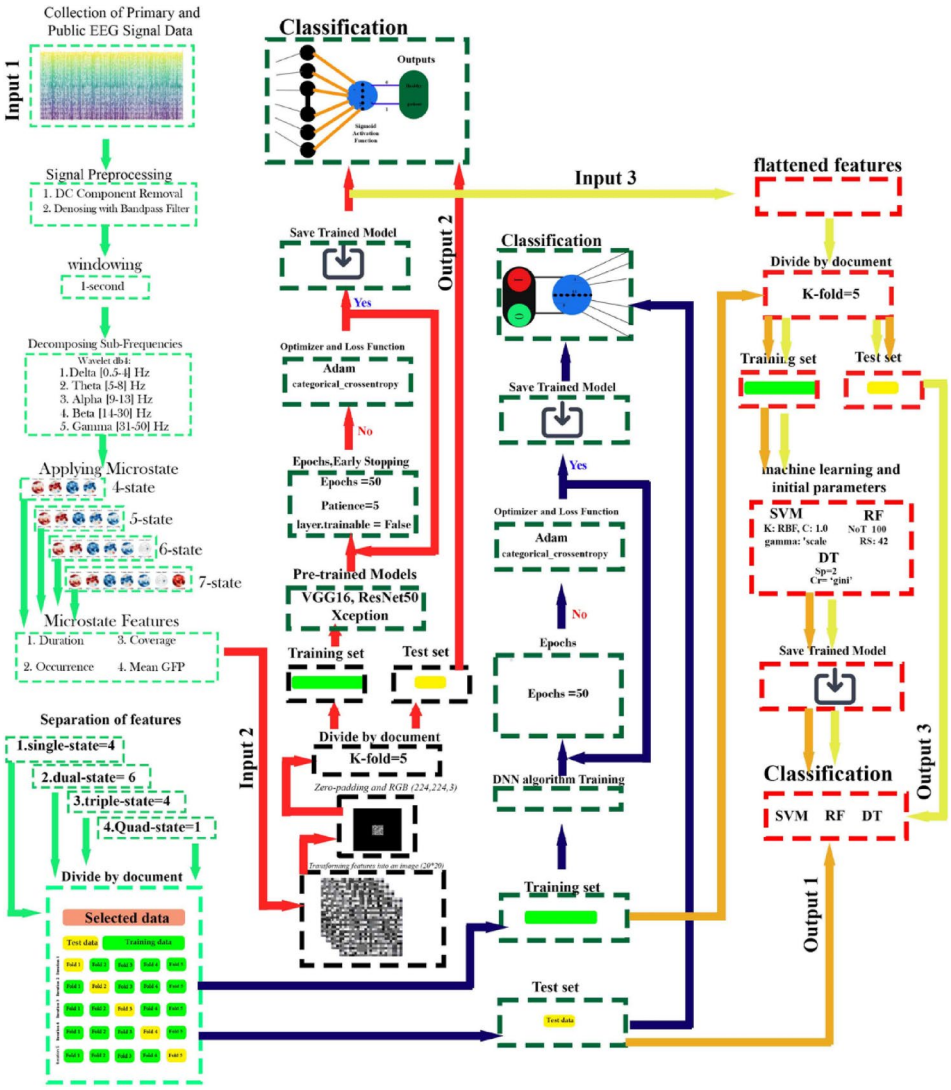


**Fig. 9**. Workflow of the proposed methodology.

## Evaluation metrics

To evaluate the performance of each model, several statistical metrics were employed. *Accuracy* represents the proportion of correct classifications across all instances. *Sensitivity (Recall)* measures the model's ability to correctly identify actual positive instances, while *Precision* indicates the proportion of true positives among all positive predictions. The *F1 Score* provides a harmonic mean of precision and recall, making it suitable for imbalanced datasets. Lastly, the *ROC Curve* visualizes diagnostic ability by plotting the True Positive Rate (TPR) against the False Positive Rate (FPR) at different thresholds, and the Area Under the Curve (AUC) summarizes the model's overall accuracy, with values closer to 1 indicating higher performance[53].

$$Accuracy = \frac{TP + TN}{TP + TN + FP + FN} \tag{12}$$

$$Sensitivity\ (Recall) = \frac{TP}{TP + FN} \tag{13}$$

$$Precision = \frac{TP}{TP + FP} \tag{14}$$

$$F1\ Score = 2 \times \frac{Precision \cdot Recall}{Precision + Recall} \tag{15}$$

$$TPR = \frac{TP}{TP + FN}, \quad FPR = \frac{FP}{FP + TN} \tag{16}$$

# Result

## EEG data acquisition and preprocessing

In this study, EEG recordings were collected from two datasets. The first dataset included EEG recordings from 64 channels at a sampling rate of 1200 Hz over a total period of 10 min, comprising 5 min with closed eyes and 5 min with open eyes, from 16 healthy participants and 20 participants with tinnitus, all in a resting state. The second dataset was a publicly available dataset consisting of EEG recordings from 19 channels, obtained from 15 healthy participants and 22 participants with tinnitus in an eyes-open condition for a duration of 2 min, with a sampling rate of 256 Hz. The preprocessing steps included segmenting the signal into 1-s windows, removing DC offset by subtracting the mean signal from the original, and eliminating electrical noise and eye blinks using a third-order Butterworth band-pass filter in the 0.5–50 Hz range. The signal was decomposed into five sub-bands: delta (0.5 to 4 Hz), theta (5 to 8 Hz), alpha (9 to 13 Hz), beta (14 to 30 Hz), and gamma (31 to 50 Hz), using the Daubechies 4 wavelet as the mother wavelet. Features such as Duration (Dur), Occurrence (Occ), Mean Global Field Power (GFP), Time Coverage (TC), and Transition Probability (TP) were extracted from each of these frequency bands and categorized into four microstate configurations: 4-state (A, B, C, D), 5-state (A, B, C, D, E), 6-state (A, B, C, D, E, F), and 7-state (A, B, C, D, E, F, G).

## Microstate dynamics comparison

Figure 10 presents the average values of four extracted microstate features (Duration, Occurrence, Mean GFP, and Coverage) for EEG microstate configurations with four-state (A, B, C, D), five-state (A, B, C, D, E), six-state (A, B, C, D, E, F), and seven-state (A, B, C, D, E, F, G) decompositions. The analysis is conducted for two subject groups, healthy and tinnitus patients, with EEG signals further decomposed into five frequency sub-bands (delta, theta, alpha, beta, gamma).

Panel (a) illustrates the feature comparison between the two groups in the eyes-closed condition, while panel (b) represents the same analysis in the eyes-open condition. Each subplot corresponds to one microstate feature under a specific microstate configuration and frequency sub-band. The x-axis represents the combination of frequency sub-bands with microstate configurations, where healthy and tinnitus groups are color-coded. The y-axis denotes the mean feature values across all EEG channels and subjects. Red stars above bars indicate the most significant differences between the two groups for each feature. Table 4 summarizes the key findings from Fig. 10, highlighting significant differences in EEG microstate parameters between healthy controls and tinnitus patients across frequency bands and conditions.

Analysis of EEG microstate dynamics revealed consistent and substantial differences between tinnitus patients and healthy controls across both eyes-closed and eyes-open conditions. Most notably, beta band microstates exhibited the most pronounced alterations, with microstate A showing increased duration (+7.8% to +11.2% ms) and microstate B showing decreased duration (−9.0% to −13.8% ms) in tinnitus patients. Occurrence rates were markedly elevated across beta band microstates in the tinnitus group (approximately 28–29% higher than controls), suggesting increased microstate transitions. These patterns remained consistent regardless of visual input state, though the magnitude of duration differences was slightly attenuated in the eyes-open condition. Additionally, specific coverage alterations were observed in microstates B and F, with Beta-7-A coverage showing a substantial 32% reduction during eyes-open in tinnitus patients. These findings point to altered cortical excitability and disrupted neural dynamics in tinnitus, particularly within frequency bands associated with cognitive processing and attention, which may reflect compensatory mechanisms or neurophysiological correlates of the tinnitus percept.

## Microstate transition probabilities

Figure 11 presents the transition probability matrices of microstates (A, B, C, D, E, F, G) for 4-state, 5-state, 6-state, and 7-state configurations in both Healthy and Tinnitus groups. Each matrix represents the probability of transitioning from one microstate to another across five sub-frequency bands: delta, theta, alpha, beta, and gamma. The results shown are derived from the combined EEG signals of all subjects within each group.

This figure illustrates the transition probabilities of EEG microstates for healthy controls and tinnitus patients in eyes-closed (a) and eyes-open (b) conditions. The left section displays topographic differences, where odd-numbered columns represent healthy individuals and even-numbered columns correspond to tinnitus patients. Each row of topographies represents a specific frequency sub-band under a given microstate configuration across all classification conditions. The right section illustrates transition networks for different microstate configurations, with blue and red colors indicating lower and higher transition probabilities, respectively. Thicker lines represent stronger transitions, and significant differences between groups are emphasized. Table 5 presents the transition probabilities of EEG microstates for healthy individuals and tinnitus patients under eyes-closed and eyes-open conditions. It highlights the most significant transitions within different frequency bands and microstate configurations. This table summarizes the key findings of Fig. 11, providing a concise comparison of transition differences between the two groups.

Analysis of microstate transition probabilities revealed distinct patterns between healthy subjects and tinnitus patients across frequency bands. The most pronounced differences were observed in the gamma band with 6 microstate configuration during eyes-closed condition (healthy: $F \rightarrow B = 0.143253$; tinnitus: $C \rightarrow D = 0.1527$; difference = 0.0095), followed by beta band with 7 microstates also during eyes-closed condition (healthy: $E \rightarrow A = 0.0913$; tinnitus: $C \rightarrow E = 0.0822$; difference = 0.0091). Similarly, in the eyes-open condition, the gamma band with 7 microstates showed substantial differences in transition patterns (healthy: $E \rightarrow A = 0.1490$; tinnitus: $C \rightarrow G = 0.1574$; difference = 0.0084). These findings suggest that higher frequency bands, particularly gamma and beta, exhibit the most discriminative transition patterns between groups, potentially reflecting altered neural synchronization mechanisms underlying tinnitus pathophysiology.


**Fig. 10**. Comparison of EEG microstate features between healthy and tinnitus subjects in eyes closed and eyes open conditions.

## Classification performance across microstates and frequency bands

Figure 12 presents the classification results using four extracted features (Duration, Occurrence, Mean GFP, and Coverage) across four microstate configurations (4-state, 5-state, 6-state, and 7-state) and five frequency bands (delta, theta, alpha, beta, and gamma) from EEG signals of two groups: healthy and tinnitus patients. The classification was performed using four models SVM, DT, RF, and DNN under both eyes-open and eyes-closed conditions. Various feature combinations were evaluated, including single-feature, two-feature, three-

| Frequency band | Microstate count | State | Parameter | Eyes closed (Healthy → Tinnitus) | % Change | Eyes open (Healthy → Tinnitus) | % Change |
|---|---|---|---|---|---|---|---|
| Beta | 4 | A | Duration (ms) | 0.3319 → 0.3690 | + 11.2% | 0.3354 → 0.3617 | + 7.8% |
| Beta | 5 | A | Duration (ms) | 0.2796 → 0.3109 | + 10.5% | 0.2692 → 0.3013 | + 7.9% |
| Beta | 4 | B | Duration (ms) | 0.2406 → 0.2160 | − 11.9% | 0.2444 → 0.2167 | − 9.0% |
| Beta | 5 | B | Duration (ms) | 0.2017 → 0.1726 | − 11.6% | 0.1986 → 0.1823 | − 9.5% |
| Beta | 6 | B | Duration (ms) | 0.1666 → 0.1477 | − 13.8% | 0.1685 → 0.1523 | − 10.3% |
| Beta | 7 | B | Duration (ms) | 0.1482 → 0.1251 | − 12.8% | 0.1458 → 0.1308 | − 11.2% |
| Beta | 4 | A | Occurrence (per sec) | 127.03 → 163.21 | + 28.1% | 126.49 → 161.44 | + 28.1% |
| Beta | 7 | A | Occurrence (per sec) | 126.74 → 161.39 | + 28.9% | – | – |
| Gamma | 7 | B | Occurrence (per sec) | – | – | 125.37 → 166.41 | + 29.2% |
| Beta | 6 | A | Mean GFP (μV) | 0.9069 → 0.9066 | − 0.03% | 0.8791 → 0.9080 | + 1.9% |
| Beta | 7 | A | Mean GFP (μV) | 0.8675 → 0.8878 | + 3.0% | 0.8540 → 0.8675 | + 2.0% |
| Gamma | 7 | A | Mean GFP (μV) | – | – | 0.7263 → 0.7016 | − 1.3% |
| Beta | 6 | B | Coverage (ratio) | 0.8999 → 0.9076 | + 1.9% | 0.8898 → 0.9134 | + 1.9% |
| Beta | 7 | B | Coverage (ratio) | 0.8910 → 0.8931 | + 0.2% | 0.8843 → 0.8746 | − 2.2% |
| Beta | 7 | F | Coverage (ratio) | 0.0501 → 0.0419 | − 19.6% | 0.0520 → 0.0426 | − 15.4% |
| Beta | 7 | A | Coverage (ratio) | – | – | 0.0025 → 0.0017 | − 32.0% |
| Theta | 7 | B | Coverage (ratio) | – | – | 0.9863 → 1.0149 | + 0.8% |

**Table 4**. Summary of significant differences in EEG microstate parameters between healthy controls and tinnitus patients in eyes-closed and eyes-open conditions.

feature, and four-feature combinations. The figure illustrates the average performance of these different feature combinations across the four models in terms of Accuracy and ROC AUC metrics. The reported results represent the mean performance over five-fold cross-validation on the test data, providing a comprehensive comparison of model effectiveness across different microstate configurations and frequency bands.

Each subplot represents one of the two metrics (accuracy and ROC-AUC) averaged across the feature configurations (single, two-feature, three-feature, and four-feature combinations). The x-axis labels correspond to the frequency bands, and the y-axis represents the model metric values. The figure highlights the classification differences and the impact of feature combinations on performance across frequency bands. Additionally, Tables 6, 7, 8, 9 summarize the classification performance under different configurations. Table 5 highlights the best performance across models and frequency bands, while Table 6 provides a comparison of classification accuracy and AUC across frequency bands. Table 7 examines the impact of the number of features on classification performance, and Table 8 explores the effect of the number of microstate configurations.

Analysis of EEG classification results for tinnitus detection revealed remarkable performance across different conditions. The highest accuracy (100%) was achieved using DNN in the gamma frequency band during open eyes condition with 5 microstates and 4 features, while in closed eyes condition, DNN with beta band features reached 96.84% accuracy. Frequency band analysis demonstrated that gamma band performed best for open eyes (99.89% accuracy, 0.9996 AUC) and beta band excelled for closed eyes (96.46% accuracy, 0.9908 AUC). Classification accuracy improved with increasing feature count, with optimal results at 4 features across all models. The number of microstates showed peak performance at 5–6 states for closed eyes and 5 states for open eyes condition, with performance degrading at higher state counts. Among classification algorithms, DNN consistently outperformed other models, though SVM showed comparable results, particularly in gamma and beta bands.

## Performance of pre-trained models and traditional classifiers

For validation, powerful pre-trained models (VGG16, ResNet50, and Xception) were utilized. The features for each subject were extracted across five frequency bands: Delta, Theta, Alpha, Beta, and Gamma, resulting in 15 images of size $20 \times 20$ for each microstate under both eyes-open and eyes-closed conditions. These images were then resized to $224 \times 224$ using zero-padding to ensure compatibility with the pre-trained models. Figure 13 presents the results of these pre-trained models combined with four classifiers: Dense Layer (DL) neural network, SVM, DT, and RF, evaluated across five performance metrics. The reported results represent the average performance obtained from a fivefold cross-validation.

Each subplot represents one of five evaluation metrics: Accuracy, F1 Score, Precision, Recall, and ROC AUC. The classifiers (SVM, DT, RF, and DL) are trained using features extracted from pretrained models (VGG16, ResNet50, and Xception), where input features are visual representations of various microstate configurations. The x-axis shows the combination of pretrained models with microstate conditions (configured with 4-state, 5-state, 6-state, or 7-state setups), while the y-axis depicts the metric scores. Table 10 provides a detailed comparison of the classification performance across deep learning models (ResNet50, Xception, and VGG16) in combination with various classifiers (DL, SVM, DT, and RF). The results include mean values and standard deviations of the five key performance metrics, separately reported for the eyes-open and eyes-closed conditions.

The results demonstrate that Xception combined with the Dense Layer (DL) classifier achieved the highest performance, particularly in the eyes-open condition, with an accuracy of $0.9996 \pm 0.0012$ and an F1-score of $0.9998 \pm 0.0018$. Similarly, ResNet50 with SVM also exhibited strong performance, reaching an accuracy of

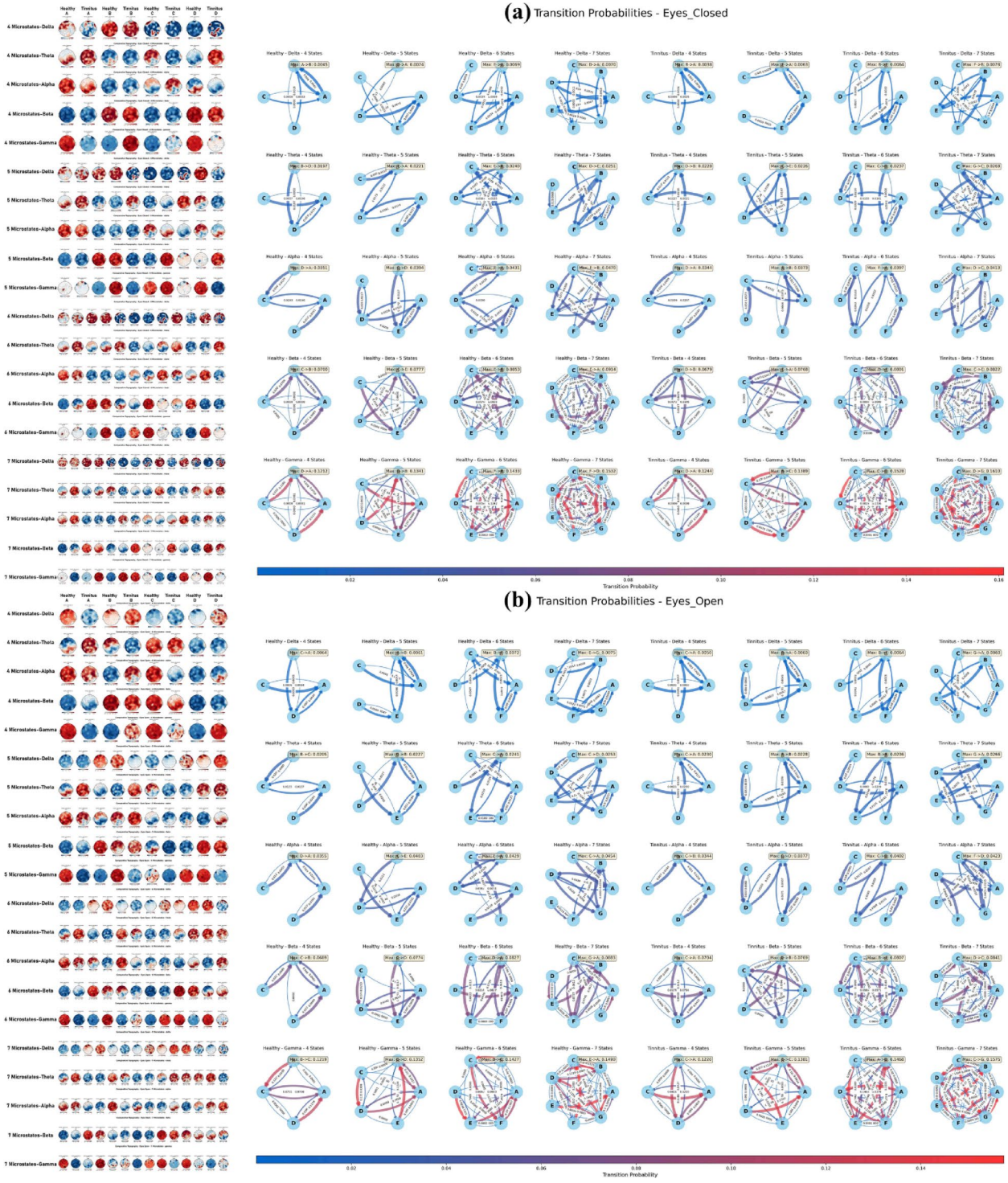


**Fig. 11**. Transition probabilities of EEG microstates in healthy controls and tinnitus patients under eyes-closed and eyes-open conditions.

0.9991 ± 0.0041 and an F1-score of 0.9993 ± 0.0035. In contrast, VGG16 underperformed across all conditions, with its best accuracy of 0.9030 ± 0.0368 using SVM in the eyes-open state. Decision Tree (DT) consistently produced the lowest scores among classifiers, particularly for VGG16, indicating its limitations in this classification task. Overall, deep learning-based classifiers outperformed traditional machine learning models, and Xception demonstrated superior generalization across both eye conditions.

To ensure generalizability and validation of the results, the extracted features from the second dataset, obtained in the eyes-open condition and converted into 20 × 20 images, were combined with the first dataset in the same condition. Figure 14 presents the classification results of four models (SVM, DL, RF, and DT) applied

| Condition | Frequency band | Number of microstates | Microstate transition (healthy) | Transition value (healthy) | Microstate transition (tinnitus) | Transition value (tinnitus) | Absolute difference |
|---|---|---|---|---|---|---|---|
| Eyes closed | Gamma | 6 | F→B | 0.143253 | C→D | 0.152776 | 0.009523 |
| | Gamma | 7 | F→D | 0.153170 | D→G | 0.161038 | 0.007868 |
| | Beta | 4 | C→B | 0.070026 | D→B | 0.067872 | 0.002154 |
| | Beta | 7 | E→A | 0.091358 | C→E | 0.082235 | 0.009123 |
| | Alpha | 5 | C→D | 0.039426 | E→B | 0.037338 | 0.002088 |
| | Alpha | 7 | F→B | 0.046957 | D→C | 0.041268 | 0.005689 |
| | Theta | 5 | E→A | 0.022147 | C→E | 0.022631 | 0.000484 |
| | Theta | 7 | D→E | 0.025058 | G→C | 0.026778 | 0.001720 |
| | Delta | 4 | A→B | 0.004473 | B→A | 0.003801 | 0.000672 |
| | Delta | 7 | D→A | 0.006993 | F→B | 0.007810 | 0.000817 |
| Eyes open | Gamma | 6 | B→C | 0.142658 | A→D | 0.146754 | 0.004096 |
| | Gamma | 7 | E→A | 0.149032 | C→G | 0.157481 | 0.008449 |
| | Beta | 4 | C→B | 0.068932 | C→A | 0.070406 | 0.001474 |
| | Beta | 7 | G→A | 0.088324 | D→C | 0.084107 | 0.004217 |
| | Alpha | 6 | E→A | 0.042926 | C→D | 0.040151 | 0.002775 |
| | Alpha | 7 | C→A | 0.045389 | F→D | 0.042312 | 0.003077 |
| | Theta | 4 | B→C | 0.020546 | C→A | 0.023046 | 0.002500 |
| | Theta | 7 | C→D | 0.025331 | G→A | 0.026561 | 0.001230 |
| | Delta | 4 | C→A | 0.006385 | C→A | 0.005018 | 0.001367 |
| | Delta | 7 | E→G | 0.007545 | G→A | 0.006025 | 0.001520 |

**Table 5**. Key transition probabilities of EEG microstates across frequency bands for healthy and tinnitus groups.

to the features extracted using three pre-trained models: Xception, ResNet50, and VGG16, for distinguishing between healthy subjects and tinnitus patients. The reported results represent the average performance over five-fold cross-validation on the test set.

Each subplot illustrates the combination of a performance metric (Accuracy or ROC AUC) with a pre-trained model to showcase the performance of the four classifiers. The x-axis represents the combination of microstate classes within different microstate configurations, while the y-axis displays the classification results in a line chart format for the four models. Table 11 summarizes the classification results for tinnitus detection using features extracted from the combined first and second datasets with three pre-trained models and four classifiers. The performance metrics across different microstate configurations (4–7) are presented, with the highest performing combinations highlighted.

Analysis of the classification results reveals that pre-trained models significantly impact tinnitus detection performance, with ResNet50 and Xception substantially outperforming VGG16 across all classifiers. The SVM classifier consistently demonstrated superior performance regardless of the feature extraction model used, achieving an average accuracy of 0.986 with ResNet50 and 0.978 with Xception. A clear pattern emerged showing performance improvement as microstate configurations increased from 4 to 6/7, with configuration 6 often offering optimal results (1.000 accuracy for ResNet50-SVM). Deep Learning classifiers showed remarkable performance with ResNet50 and Xception (0.961 and 0.953 average accuracy, respectively) but performed poorly with VGG16 features (0.617), suggesting that feature quality significantly impacts classifier effectiveness. These findings indicate that the combination of ResNet50 or Xception with SVM classifiers using higher microstate configurations (6 or 7) provides the most reliable approach for distinguishing between tinnitus patients and healthy controls from EEG data.

## Discussion

This study investigated EEG microstate dynamics in tinnitus patients compared to healthy controls utilizing two complementary datasets: a primary dataset comprising 36 participants (16 healthy, 20 tinnitus), and a public dataset of 37 participants (15 healthy, 22 tinnitus). The EEG signals were decomposed into five frequency bands (delta (0.5 to 4 Hz), theta (5 to 8 Hz), alpha (9 to 13 Hz), beta (14 to 30 Hz), and gamma (31 to 50 Hz)) using Daubechies 4 wavelet. Analysis revealed significant alterations in beta band microstates, with microstate A showing increased duration (+7.8% to +11.2%) and microstate B showing decreased duration (−9.0% to −13.8%) in tinnitus patients, while occurrence rates were markedly elevated (~28–29% higher) in the tinnitus group. Transition probability analysis identified distinctive patterns between groups, with the most pronounced differences observed in gamma band (6-state configuration) during eyes-closed condition (healthy: F→B = 0.143; tinnitus: C→D = 0.153; difference = 0.0095) and beta band (7-state configuration) also during eyes-closed condition (healthy: E→A = 0.091; tinnitus: C→E = 0.082; difference = 0.0091). Classification performance was exceptional when using microstate dynamics as discriminative features, with the highest accuracy (100%) achieved using DNN in the gamma frequency band with 5-state configuration and the combination of all four features (Duration, Occurrence, Mean GFP, and Coverage). Feature analysis demonstrated that classification accuracy

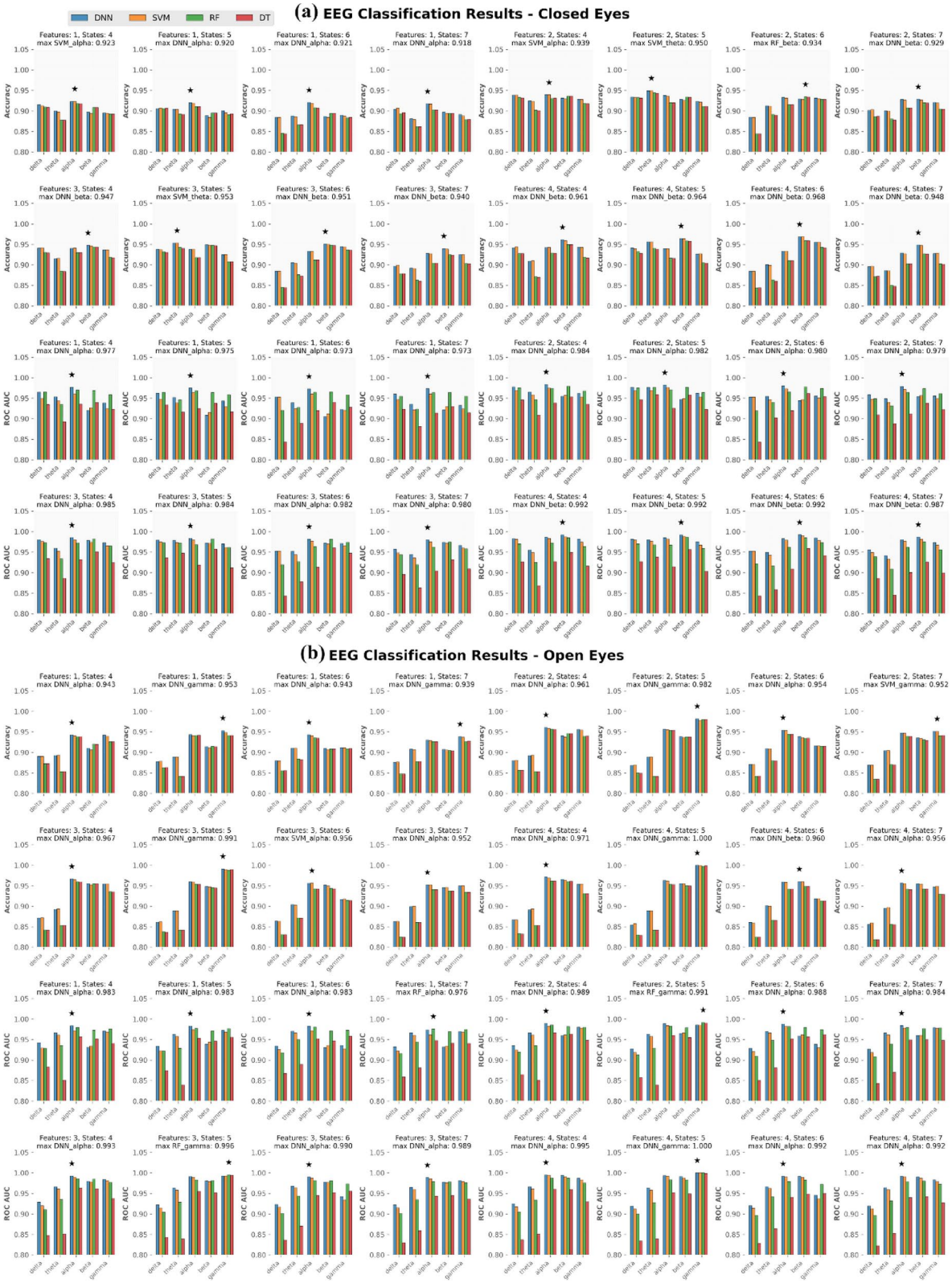


**Fig. 12**. EEG classification results across microstate configurations and frequency bands for healthy and tinnitus patients under eyes-open and eyes-closed conditions.

| Condition | Model | Frequency band | Num states | Feature count | Accuracy (%) | ROC AUC |
|---|---|---|---|---|---|---|
| Closed eyes | DNN | Beta | 6 | 4 | 96.84 | 0.9923 |
| Closed eyes | SVM | Beta | 6 | 4 | 96.83 | 0.9891 |
| Closed eyes | RF | Beta | 6 | 4 | 95.92 | 0.9846 |
| Closed eyes | DT | Beta | 5 | 4 | 95.75 | 0.9566 |
| Open eyes | DNN | Gamma | 5 | 4 | 100.00 | 1.0000 |
| Open eyes | SVM | Gamma | 5 | 4 | 99.93 | 1.0000 |
| Open eyes | DT | Gamma | 5 | 4 | 99.85 | 0.9983 |
| Open eyes | RF | Gamma | 5 | 4 | 99.78 | 0.9999 |

**Table 6**. Best performance across models and frequency bands.

| Frequency band | Closed eyes accuracy (%) | Closed eyes AUC | Open eyes accuracy (%) | Open eyes AUC |
|---|---|---|---|---|
| Delta | 94.01 ± 0.44 | 0.9809 ± 0.0016 | 89.33 ± 0.82 | 0.9298 ± 0.0039 |
| Theta | 95.30 ± 0.39 | 0.9767 ± 0.0031 | 90.67 ± 0.81 | 0.9661 ± 0.0031 |
| Alpha | 94.15 ± 0.45 | 0.9843 ± 0.0018 | 96.87 ± 0.48 | 0.9924 ± 0.0021 |
| Beta | 96.46 ± 0.32 | 0.9908 ± 0.0018 | 96.20 ± 0.48 | 0.9889 ± 0.0029 |
| Gamma | 95.55 ± 0.53 | 0.9834 ± 0.0052 | 99.89 ± 0.10 | 0.9996 ± 0.0002 |

**Table 7**. Performance comparison across frequency bands (average of best performances).

| Feature count | Closed eyes accuracy (%) | Closed eyes AUC | Open eyes accuracy (%) | Open eyes AUC |
|---|---|---|---|---|
| 1 | 89.51 ± 1.83 | 0.9420 ± 0.0206 | 91.15 ± 2.64 | 0.9461 ± 0.0235 |
| 2 | 92.19 ± 1.69 | 0.9610 ± 0.0158 | 93.10 ± 2.58 | 0.9625 ± 0.0201 |
| 3 | 93.13 ± 1.51 | 0.9696 ± 0.0134 | 93.90 ± 2.51 | 0.9703 ± 0.0193 |
| 4 | 93.72 ± 1.46 | 0.9750 ± 0.0128 | 94.32 ± 2.47 | 0.9750 ± 0.0187 |

**Table 8**. Effect of feature count on classification performance (average across models).

| Num states | Closed eyes accuracy (%) | Closed eyes AUC | Open eyes accuracy (%) | Open eyes AUC |
|---|---|---|---|---|
| 4 | 93.68 ± 1.49 | 0.9697 ± 0.0147 | 94.76 ± 2.45 | 0.9720 ± 0.0200 |
| 5 | 93.82 ± 1.53 | 0.9704 ± 0.0151 | 94.99 ± 2.49 | 0.9746 ± 0.0191 |
| 6 | 92.03 ± 1.72 | 0.9560 ± 0.0188 | 93.23 ± 2.51 | 0.9605 ± 0.0210 |
| 7 | 90.64 ± 1.81 | 0.9497 ± 0.0203 | 91.32 ± 2.55 | 0.9505 ± 0.0225 |

**Table 9**. Effect of number of states on classification performance (average across models).

improved with increasing feature count, with optimal results consistently achieved using the combination of all four features across models (93.72% accuracy in closed-eyes, 94.32% in open-eyes condition). Validation with pre-trained deep learning models showed that ResNet50 with SVM classifier using 6-state configurations provided optimal discrimination (100% accuracy), while frequency band analysis confirmed gamma band excelled for open eyes (99.89% accuracy) and beta band for closed eyes (96.46% accuracy), suggesting altered cortical excitability and disrupted neural dynamics in tinnitus.

Our study on EEG microstate dynamics in tinnitus patients contributes significant novel insights to the growing body of research on neurophysiological markers of tinnitus. The findings align with several recent studies while offering unique methodological advancements and results. Mai Jianbiao et al.[25] demonstrated significant differences in sample entropy values across multiple frequency bands in tinnitus patients, particularly in delta, alpha2, and beta1 bands, achieving 91.38% classification accuracy using wavelet transform and sample entropy. Similarly, our study identified significant alterations in beta and gamma band microstates, suggesting altered cortical excitability in tinnitus patients. The microstate alterations observed in our research, particularly increased duration of microstate A (+7.8% to +11.2%) and decreased duration of microstate B (−9.0% to −13.8%) in tinnitus patients, share interesting parallels with Yuexin Cai's studies[18,19]. Cai reported an increased presence of class A microstate and decreased presence of class D microstate in tinnitus patients, as well as altered syntax patterns. Our work extends these findings by providing more granular analysis across multiple frequency bands and demonstrating substantially higher classification accuracy. A notable strength of our methodology is the exceptional classification performance achieved using microstate dynamics as discriminative features,

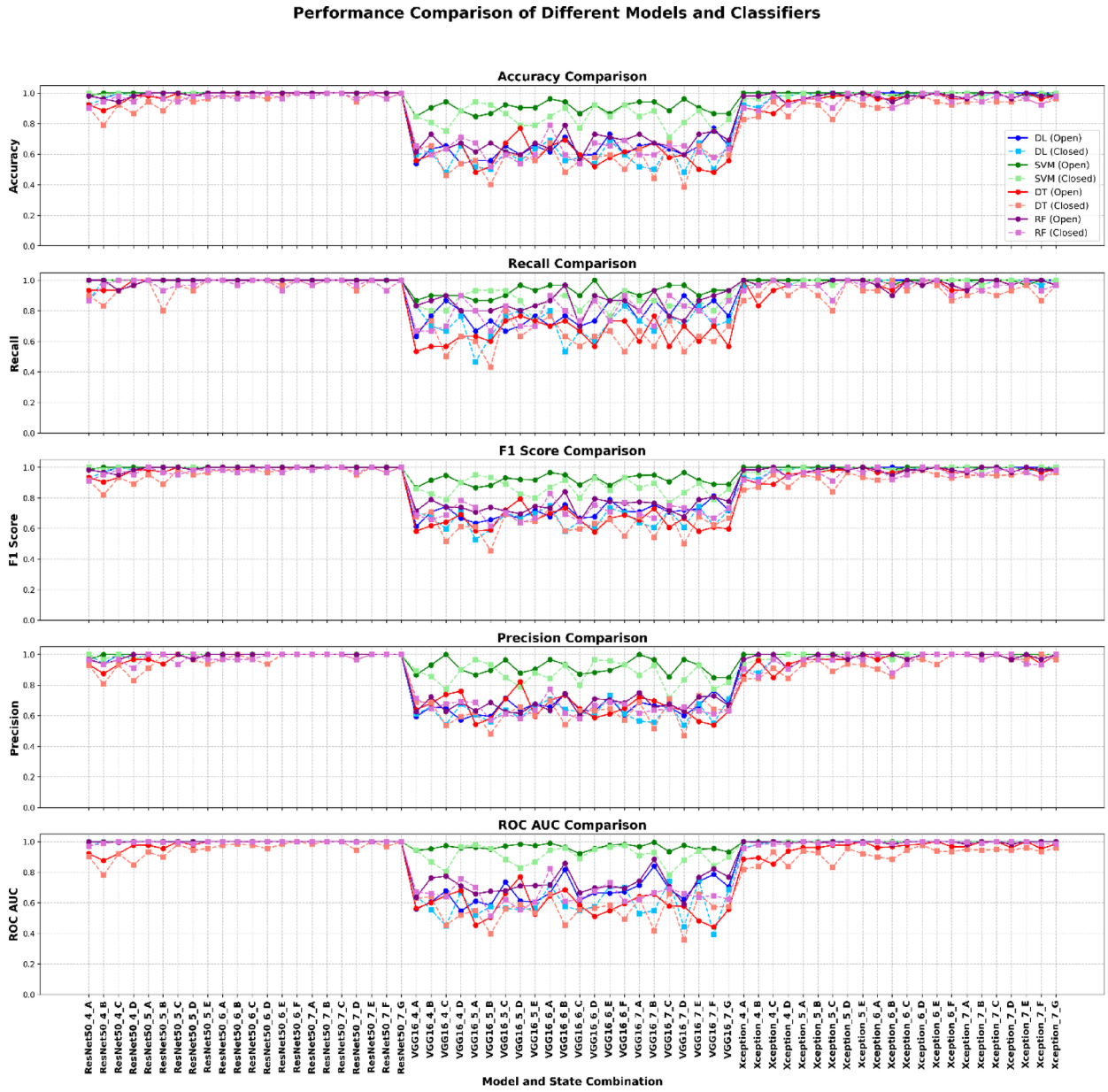


**Fig. 13**. Comparative analysis of microstate classification performance across models and classifiers under eyes-open and eyes-closed conditions.

with 100% accuracy using DNN in the gamma frequency band with 5-state configuration. This surpasses the accuracy reported in previous studies, such as Chang-Dong Wang's[54] MECRL framework (91.24%), Su Zhou's[24] DNN model (92%), and even approaches the high accuracy reported by Zhi-Ran Sun[23] at 99.23%. While a direct comparison with recent advances such as Awais et al.'s[55] graph neural network approach (which achieved 99.41% accuracy) is challenging due to differences in datasets, methodology, and experimental conditions, our approach offers distinct advantages in capturing temporal dynamics of brain states. Awais et al. innovatively represented EEG channels as graph networks, enabling the modeling of complex inter-channel relationships using Graph Convolutional Networks combined with LSTM networks. Our microstate-based approach captures complementary aspects of brain dynamics, focusing on global brain states rather than channel-wise relationships. Future research combining microstate dynamics with graph-based topological features across standardized datasets might yield even more robust classification frameworks for tinnitus. Our study's innovative use of wavelet decomposition into five frequency bands provides more comprehensive insights than studies focusing on fewer bands. For instance, Eul-Seok Hong et al.[25] primarily identified alpha activity as crucial for identifying tinnitus patients, while our analysis revealed significant alterations in beta and gamma bands specifically. This multi-band approach allows for more targeted identification of frequency-specific neural signatures of tinnitus. The observation that gamma band excelled for open eyes (99.89% accuracy) and beta band for closed eyes (96.46% accuracy) represents a novel contribution to understanding state-dependent tinnitus markers. This

| Model | Classifier | Eye condition | Accuracy | Recall | F1 score | Precision | ROC AUC |
|---|---|---|---|---|---|---|---|
| ResNet50 | DL | Open | 0.9974 ± 0.0090 | 0.9998 ± 0.0014 | 0.9978 ± 0.0076 | 0.9957 ± 0.0147 | 0.9998 ± 0.0012 |
| ResNet50 | SVM | Open | 0.9991 ± 0.0041 | 0.9997 ± 0.0032 | 0.9993 ± 0.0035 | 0.9985 ± 0.0069 | 0.9998 ± 0.0024 |
| ResNet50 | DT | Open | 0.9834 ± 0.0321 | 0.9909 ± 0.0234 | 0.9858 ± 0.0273 | 0.9810 ± 0.0335 | 0.9820 ± 0.0341 |
| ResNet50 | RF | Open | 0.9930 ± 0.0152 | 0.9955 ± 0.0156 | 0.9940 ± 0.0132 | 0.9927 ± 0.0169 | 0.9996 ± 0.0014 |
| Xception | DL | Open | 0.9996 ± 0.0012 | 0.9998 ± 0.0028 | 0.9998 ± 0.0018 | 0.9998 ± 0.0016 | 0.9998 ± 0.0010 |
| Xception | SVM | Open | 0.9974 ± 0.0068 | 0.9955 ± 0.0117 | 0.9977 ± 0.0060 | 0.9984 ± 0.0045 | 0.9987 ± 0.0041 |
| Xception | DT | Open | 0.9633 ± 0.0365 | 0.9697 ± 0.0397 | 0.9683 ± 0.0313 | 0.9686 ± 0.0430 | 0.9621 ± 0.0389 |
| Xception | RF | Open | 0.9799 ± 0.0201 | 0.9788 ± 0.0263 | 0.9825 ± 0.0174 | 0.9868 ± 0.0233 | 0.9963 ± 0.0065 |
| VGG16 | DL | Open | 0.6302 ± 0.0596 | 0.7697 ± 0.0769 | 0.7055 ± 0.0477 | 0.6550 ± 0.0505 | 0.6696 ± 0.0794 |
| VGG16 | SVM | Open | 0.9030 ± 0.0368 | 0.9212 ± 0.0392 | 0.9166 ± 0.0312 | 0.9139 ± 0.0482 | 0.9621 ± 0.0192 |
| VGG16 | DT | Open | 0.5970 ± 0.0745 | 0.6545 ± 0.0774 | 0.6519 ± 0.0599 | 0.6559 ± 0.0742 | 0.5866 ± 0.0823 |
| VGG16 | RF | Open | 0.6713 ± 0.0590 | 0.8439 ± 0.0662 | 0.7474 ± 0.0457 | 0.6725 ± 0.0451 | 0.7246 ± 0.0697 |
| ResNet50 | DL | Closed | 0.9939 ± 0.0182 | 0.9939 ± 0.0284 | 0.9945 ± 0.0166 | 0.9957 ± 0.0147 | 0.9985 ± 0.0062 |
| ResNet50 | SVM | Closed | 0.9983 ± 0.0057 | 0.9993 ± 0.0042 | 0.9985 ± 0.0048 | 0.9971 ± 0.0095 | 0.9989 ± 0.0083 |
| ResNet50 | DT | Closed | 0.9528 ± 0.0530 | 0.9591 ± 0.0553 | 0.9591 ± 0.0456 | 0.9614 ± 0.0551 | 0.9517 ± 0.0552 |
| ResNet50 | RF | Closed | 0.9738 ± 0.0256 | 0.9758 ± 0.0344 | 0.9771 ± 0.0226 | 0.9794 ± 0.0268 | 0.9964 ± 0.0069 |
| Xception | DL | Closed | 0.9851 ± 0.0251 | 0.9909 ± 0.0152 | 0.9874 ± 0.0209 | 0.9844 ± 0.0326 | 0.9967 ± 0.0094 |
| Xception | SVM | Closed | 0.9895 ± 0.0129 | 0.9924 ± 0.0143 | 0.9910 ± 0.0111 | 0.9898 ± 0.0181 | 0.9994 ± 0.0014 |
| Xception | DT | Closed | 0.9205 ± 0.0445 | 0.9288 ± 0.0528 | 0.9309 ± 0.0384 | 0.9358 ± 0.0532 | 0.9189 ± 0.0467 |
| Xception | RF | Closed | 0.9554 ± 0.0358 | 0.9636 ± 0.0340 | 0.9617 ± 0.0304 | 0.9611 ± 0.0440 | 0.9911 ± 0.0108 |
| VGG16 | DL | Closed | 0.5830 ± 0.0718 | 0.7121 ± 0.0946 | 0.6619 ± 0.0626 | 0.6240 ± 0.0586 | 0.5917 ± 0.0986 |
| VGG16 | SVM | Closed | 0.8418 ± 0.0644 | 0.8591 ± 0.0581 | 0.8628 ± 0.0539 | 0.8697 ± 0.0709 | 0.9076 ± 0.0576 |
| VGG16 | DT | Closed | 0.5612 ± 0.0843 | 0.6333 ± 0.0891 | 0.6240 ± 0.0742 | 0.6179 ± 0.0731 | 0.5481 ± 0.0872 |
| VGG16 | RF | Closed | 0.6267 ± 0.0619 | 0.7818 ± 0.0847 | 0.7063 ± 0.0521 | 0.6473 ± 0.0474 | 0.6518 ± 0.0657 |

**Table 10**. Comprehensive comparison of deep learning models combined with classifiers based on key performance metrics across eyes-open and eyes-closed conditions.

finding aligns with Yingying Wang's[56] observation that microstate parameters significantly differed between open-eyes and closed-eyes states in tinnitus patients, though our study provides more specific frequency-related insights. A particular strength of our methodology is the use of two complementary datasets and the careful consideration of both eyes-open and eyes-closed conditions. This robust approach addresses limitations noted in studies like Min Zhu's[57], which focused primarily on eyes-closed conditions. The transition probability analysis identifying distinctive patterns between groups, with pronounced differences in gamma and beta bands, offers new insights into the dynamic neural reorganization in tinnitus. A key distinction between our work and Ke's studies is in computational efficiency. While Ke's[46,58] approaches demonstrate impressive processing speeds (classification "several hundred times faster than EEG being collected"), our focus was on optimizing classification accuracy through comprehensive feature extraction across multiple frequency bands. Future work could integrate Ke's efficient architecture design principles with our microstate-based feature extraction to create systems suitable for real-time tinnitus detection and monitoring. However, our study has certain limitations. Unlike Maryam Doborjeh's[26] research, which linked EEG features to therapy outcomes, our study focused on diagnostic classification rather than treatment response prediction. Additionally, while Muhammad Awais[55] employed graph neural networks to model relationships between EEG channels, our approach did not explicitly model inter-channel relationships, which could provide additional insights into tinnitus-related network disruptions. The exceptional classification accuracy achieved in our study (100% in optimal configurations) warrants cautious interpretation and further validation across diverse tinnitus populations. Nevertheless, the consistency of our findings across two independent datasets strengthens the reliability of our results and suggests that EEG microstate dynamics, particularly in beta and gamma bands, may serve as robust biomarkers for tinnitus, potentially advancing both diagnosis and treatment evaluation approaches.

The observed alterations in EEG microstate dynamics, particularly in the beta band as illustrated in Fig. 10 and summarized in Table 4, suggest significant neurophysiological differences in cortical functioning between tinnitus patients and healthy controls. The consistent pattern of increased microstate A duration (+7.8% to +11.2%) and decreased microstate B duration (−9.0% to −13.8%), coupled with markedly elevated occurrence rates (~28–29% higher) in tinnitus patients, aligns with previous findings by Vanneste et al.[59] who reported aberrant beta band activity in tinnitus-related neural networks. These microstate alterations may reflect disrupted inhibitory mechanisms and hyperexcitability in auditory processing pathways, consistent with the thalamocortical dysrhythmia model proposed by De Ridder et al.[60], which posits that tinnitus emerges from abnormal oscillatory activity following deafferentation of peripheral auditory input. Furthermore, the substantial 32% reduction in Beta-7-A coverage during eyes-open conditions in tinnitus patients suggests altered attentional resource allocation, supporting Czornik et al.'s[61] findings that tinnitus involves reorganization of large-scale brain networks beyond purely auditory regions. These microstate abnormalities likely represent

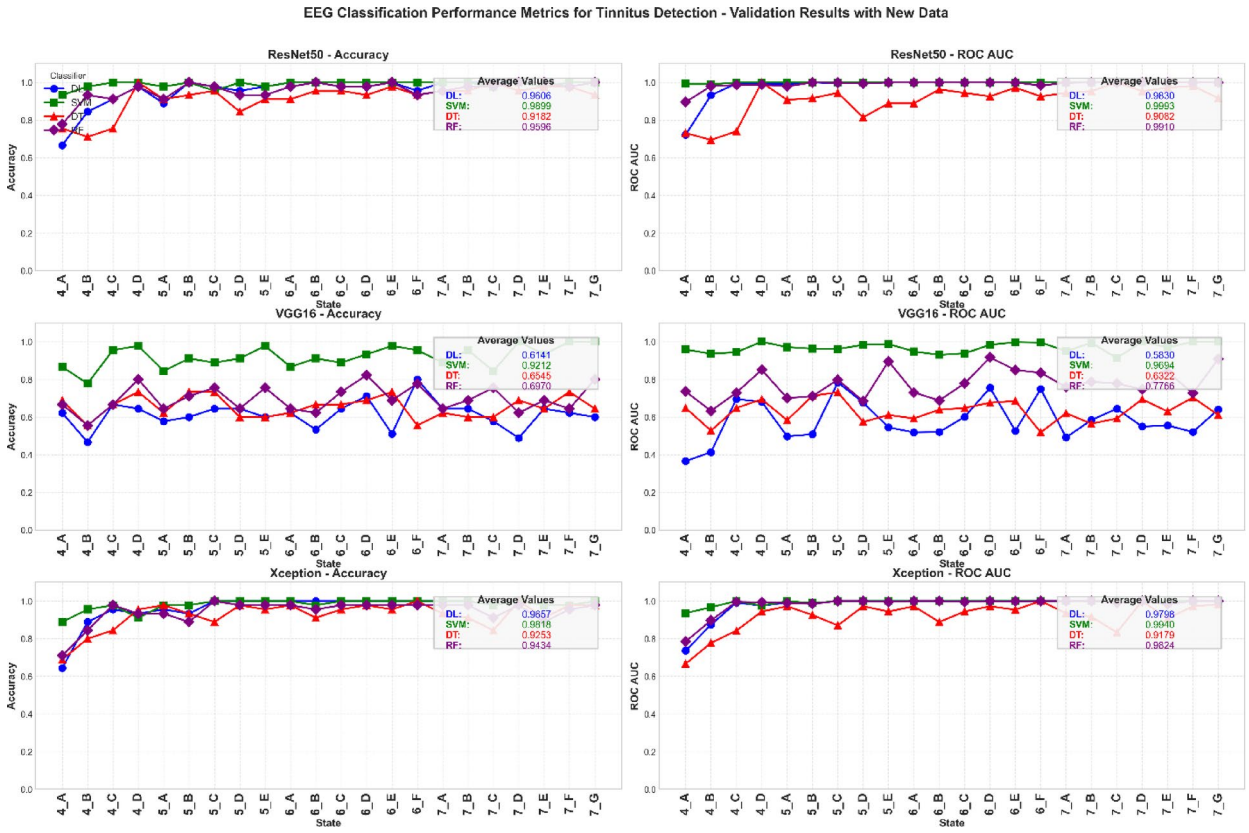


**Fig. 14**. EEG-based classification of tinnitus using pre-trained deep learning models and machine learning classifiers with validation on an independent dataset.

| Pre-trained model | Classifier | Average accuracy | Average ROC AUC | Average by microstate configuration (accuracy) |
|---|---|---|---|---|
| ResNet50 | DL | 0.961 | 0.989 | 4: 0.850, 5: 0.960, 6: 0.991, 7: 0.996 |
| ResNet50 | SVM | 0.986 | 0.997 | 4: 0.978, 5: 0.982, 6: 1.000, 7: 0.994 |
| ResNet50 | DT | 0.913 | 0.903 | 4: 0.819, 5: 0.925, 6: 0.952, 7: 0.965 |
| ResNet50 | RF | 0.953 | 0.991 | 4: 0.900, 5: 0.951, 6: 0.977, 7: 0.984 |
| Xception | DL | 0.953 | 0.979 | 4: 0.856, 5: 0.978, 6: 0.996, 7: 0.994 |
| Xception | SVM | 0.978 | 0.996 | 4: 0.933, 5: 0.991, 6: 0.996, 7: 0.994 |
| Xception | DT | 0.909 | 0.897 | 4: 0.847, 5: 0.946, 6: 0.957, 7: 0.937 |
| Xception | RF | 0.930 | 0.968 | 4: 0.866, 5: 0.965, 6: 0.974, 7: 0.952 |
| VGG16 | DL | 0.617 | 0.582 | 4: 0.600, 5: 0.613, 6: 0.644, 7: 0.596 |
| VGG16 | SVM | 0.912 | 0.969 | 4: 0.894, 5: 0.907, 6: 0.922, 7: 0.917 |
| VGG16 | DT | 0.655 | 0.640 | 4: 0.661, 5: 0.658, 6: 0.655, 7: 0.648 |
| VGG16 | RF | 0.698 | 0.777 | 4: 0.672, 5: 0.702, 6: 0.715, 7: 0.692 |

**Table 11**. Performance comparison of pre-trained models and classifiers for tinnitus detection using combined datasets across different microstate configurations.

both compensatory mechanisms and direct neurophysiological correlates of the phantom auditory perception, providing potential biomarkers for tinnitus diagnosis and treatment monitoring.

The analysis of microstate transition probabilities presented in Fig. 11 reveals critical neurophysiological differences in tinnitus pathophysiology, particularly in higher frequency bands. As detailed in Table 5, the most pronounced differences were observed in gamma band (6-state configuration) during eyes-closed condition (healthy: $F \rightarrow B = 0.143$; tinnitus: $C \rightarrow D = 0.153$; difference = 0.0095) and beta band (7-state configuration) also during eyes-closed condition (healthy: $E \rightarrow A = 0.091$; tinnitus: $C \rightarrow E = 0.082$; difference = 0.0091). These findings align with De Ridder et al.'s[60] thalamocortical dysrhythmia model, which posits that tinnitus involves dysfunctional gamma-band activity reflecting abnormal thalamocortical oscillations. Moreover, Fig. 11 illustrates distinct transition patterns in the eyes-open condition, particularly in gamma band with 7 microstates (healthy: $E \rightarrow A = 0.149$; tinnitus: $C \rightarrow G = 0.157$; difference = 0.0084), supporting Sedley et al.'s[62] predictive coding

framework, which proposes that tinnitus results from aberrant precision weighting of sensory prediction errors, manifested as irregular gamma oscillations. The preferential involvement of higher frequency bands in discriminating between healthy and tinnitus groups, as evident from Table 5, corroborates Weisz et al.'s[63] findings of increased gamma activity in tinnitus patients, suggesting that these altered transition probabilities reflect disrupted neural synchronization mechanisms underlying phantom sound perception. These microstate transition abnormalities may represent neurophysiological markers of the maladaptive neuroplastic changes in tinnitus, providing insight into the dynamic cortical reorganization that occurs in this condition.

The exceptional classification performance demonstrated in our study (Fig. 12, Tables 6, 7, 8, 9) suggests that EEG microstate dynamics provide robust biomarkers for differentiating between tinnitus patients and healthy controls. The perfect accuracy (100%) achieved by DNN with gamma band features during the eyes-open condition with 5-state configuration highlights the discriminative power of microstate parameters in capturing the neurophysiological signature of tinnitus. This finding aligns with Elsa van et al.[64], who reported altered gamma oscillations in tinnitus patients, potentially reflecting thalamocortical dysrhythmia and aberrant neural synchrony in auditory cortical regions. The frequency-specific classification performance, particularly the superiority of gamma band for eyes-open (99.89% accuracy) and beta band for eyes-closed conditions (96.46% accuracy) as shown in Table 6, suggests state-dependent alterations in cortical processing. The gamma band's exceptional performance during eyes-open condition supports the notion proposed by Sedley et al.[65] that tinnitus involves heightened perceptual salience processing, which is predominantly mediated by gamma oscillations. Conversely, the beta band's efficacy during eyes-closed condition aligns with Weisz et al.[66], who identified beta band abnormalities as markers of altered inhibitory control in tinnitus. The progressive improvement in classification accuracy with increasing feature count (Table 9) underscores the multidimensional nature of tinnitus-related EEG alterations. The optimal performance achieved with all four features (Duration, Occurrence, Mean GFP, and Coverage) suggests that these parameters collectively capture complementary aspects of the underlying neurophysiological abnormalities. Each feature provides unique information. Duration and Occurrence describe the temporal dynamics, while Coverage and Mean GFP reflect the spatial engagement and intensity of brain activity. Their combined use enhances the model's ability to distinguish between healthy and pathological patterns more effectively than using any single feature alone. This multidimensional characterization of tinnitus is consistent with current network models that conceptualize tinnitus as a complex disorder involving multiple brain systems beyond just auditory pathways[67]. The optimal performance observed with 5–6 state configurations (Table 9) provides insights into the spatial complexity of tinnitus-related brain activity. This finding suggests that while excessive spatial complexity (7 states) may introduce noise, insufficient state counts (4 states) may fail to capture the full spectrum of altered network dynamics. The algorithmic comparison revealing DNN's superiority, though with SVM showing comparable results, demonstrates the value of both linear and non-linear classification approaches in tinnitus detection. These findings collectively support the clinical potential of EEG microstate analysis as a diagnostic tool for tinnitus and offer new insights into the neural mechanisms underlying this condition.

The outstanding performance of pre-trained deep learning models in tinnitus detection (Fig. 13, Table 10) highlights the efficacy of transfer learning in neurophysiological biomarker identification. Our novel transformation of microstate features into 2D image representations ($20 \times 20$ pixels) enabled the application of CNN architectures, capturing multidimensional relationships across frequency bands. The near-perfect classification accuracies of Xception-DL (99.96%) and ResNet50-SVM (99.91%) in the eyes-open condition suggest that these models effectively distinguish tinnitus-related microstate patterns. These results align with prior studies[68], demonstrating the ability of CNNs to extract discriminative features from neuroimaging data. ResNet50 and Xception consistently outperformed VGG16 across classifiers, emphasizing the advantages of deeper architectures with residual connections in interpreting complex EEG microstate representations. Validation on an independent dataset (Fig. 14, Table 11) confirmed the generalizability of these findings, with ResNet50-SVM achieving 100% accuracy in the 6-state microstate configuration, suggesting that the identified biomarkers reflect fundamental neurophysiological alterations rather than dataset-specific variations. The image-based representation method ($20 \times 20$ pixel matrices resized to $224 \times 224$ via zero-padding) effectively preserved discriminative features, enhancing CNN compatibility. Increasing microstate configurations (from 4 to 6/7 states) progressively improved classification performance, indicating an optimal granularity for capturing tinnitus-related network dynamics. This observation aligns with previous findings[69], where higher-dimensional EEG representations better characterized altered functional connectivity in auditory disorders. The superior performance of SVM classifiers, particularly in combination with ResNet50 features, underscores the effectiveness of support vector boundaries in distinguishing tinnitus-related neural signatures. The differential classification performance between eyes-open and eyes-closed conditions suggests state-dependent alterations in tinnitus-related neural activity. The generally higher accuracies in the eyes-open condition, especially with Xception, may reflect enhanced salience processing and attention mechanisms during sensory engagement. The 2D spatial representation strategy preserved key topological relationships among microstate parameters, effectively capturing these differences. This aligns with findings[70] suggesting that tinnitus involves abnormal interactions between attention and auditory processing networks, which are more pronounced during sensory processing. Overall, the remarkable classification accuracy achieved through deep learning on 2D microstate representations provides a promising diagnostic framework for tinnitus. Moreover, these findings offer computational evidence of distinct neural patterns underlying the condition, which could inform targeted neuromodulation therapies aimed at normalizing aberrant network dynamics.

In recent years, transforming EEG-derived data into image-based representations has become a promising strategy for utilizing the capabilities of pre-trained convolutional neural networks (CNNs) in classification tasks. This direction has been significantly motivated by studies that construct images from effective brain connectivity matrices, such as the Directed Transfer Function (dDTF) and Transfer Entropy (TE), which aim to

capture the directional flow of information among EEG channels and represent inter-regional interactions[41,42]. While such connectivity-based methods primarily focus on spatial relationships between EEG channels, the approach proposed in this study introduces an alternative perspective by emphasizing temporal microstate dynamics across different frequency bands. Our feature-to-image transformation does not reflect the spatial structure of the brain but rather encapsulates the temporal evolution of brain functional states over time, which is particularly relevant in understanding disorders characterized by abnormal temporal neural patterns, such as tinnitus. We selected four microstate-derived features (Duration, Occurrence, Mean Global Field Power (GFP), and Coverage) based on their solid theoretical grounding and consistent use in the literature on EEG microstate analysis. These features provide a quantitative summary of the stability, frequency, and intensity of transient brain states and have demonstrated discriminative power in studies involving neuropsychiatric populations including schizophrenia, depression, and tinnitus. The primary motivation behind converting these features into two-dimensional grayscale images lies in facilitating compatibility with CNN architectures. This transformation allows the models to exploit spatial feature extraction capabilities to identify latent patterns and correlations that traditional machine learning approaches may fail to capture. In the generated images, each row represents a one-second EEG segment, while each column corresponds to a specific feature computed under a given frequency band and microstate configuration. This structure preserves temporal information across samples while enabling the learning of frequency-specific feature representations. In summary, the proposed framework extends existing methodologies by integrating temporal microstate dynamics into an image-based representation paradigm. Rather than focusing on spatial connectivity patterns, as demonstrated in prior studies[41,42], our method highlights time-resolved neurophysiological features, offering new insights into the temporal organization of brain activity in tinnitus and providing a complementary direction for EEG-based deep learning applications.

In this study, computational models were implemented using Python, with TensorFlow and Keras employed for constructing and training neural networks. Simulations were performed on a system featuring an NVIDIA RTX 3050 Ti laptop GPU with 4GB VRAM to enhance training speed, along with an Intel Core i7 processor, 32GB of RAM, and Windows 11 as the operating system. PyCharm was used as the integrated development environment (IDE), and additional libraries such as NumPy, pandas, and SciPy facilitated data preprocessing and analysis. Over the 48 h required to classify all combined microstates across various frequency bands shown in Fig. 10, DT achieved a classification speed approximately 750 times faster than DNN, SVM was 60 times faster than DNN, and RF demonstrated a 30 times improvement in speed over DNN. These results highlight the efficiency of different classifiers in analyzing microstates, underscoring how computational optimizations can significantly reduce processing time.

The clinical and research applications of our findings offer meaningful potential for advancing tinnitus management approaches. Our microstate-based methodology, particularly the identification of specific beta and gamma band abnormalities, provides a neurophysiological framework that could inform personalized intervention strategies. The high classification accuracy achieved suggests these EEG patterns may serve as useful biomarkers for earlier tinnitus detection, potentially identifying cases before subjective symptoms become more severe. These distinctive microstate signatures could guide neurofeedback protocols where patients might be trained to modulate altered beta and gamma band dynamics, addressing the underlying cortical excitability changes. Regarding computational efficiency, our analysis revealed substantial differences in processing speeds among classifiers, with Decision Trees performing approximately 750 times faster than DNNs, SVMs 60 times faster, and Random Forests 30 times faster. These efficiency differences are critically important for potential clinical applications, as they directly impact the feasibility of real-time assessment. While DNNs achieved marginally higher accuracy, the substantially faster traditional classifiers (particularly SVMs with ResNet50 features) may represent a more practical balance between performance and speed for clinical implementation, enabling point-of-care assessment without requiring specialized computational resources.

Despite the promising results, several limitations should be acknowledged in this study. While our combined datasets provided a reasonable sample size (n = 73), the heterogeneity of tinnitus presentations and relatively limited demographic diversity may restrict the generalizability of our findings to broader populations. The varying EEG acquisition protocols between datasets (64-channel vs. 19-channel systems, different sampling rates) highlight the need for standardization in EEG methodology for tinnitus assessment, as these technical differences could influence microstate derivation and subsequent analysis. Future research should address these limitations through longitudinal studies examining the temporal stability of microstate markers over time, which would establish their reliability as biomarkers and potentially track disease progression. Moreover, investigating longitudinal treatment responses and the effects of therapeutic interventions on microstate dynamics could provide valuable insights into their potential as objective markers for monitoring clinical outcomes. Additionally, comparative studies with other neurological disorders sharing similar symptoms (e.g., hyperacusis, chronic pain) would help determine the specificity of these microstate patterns to tinnitus. Integration of this approach with complementary neuroimaging techniques like fMRI could provide multimodal validation and establish more precise relationships between microstate dynamics and underlying neural network alterations, advancing our understanding of the neurophysiological mechanisms of tinnitus. Moreover, incorporating advanced deep learning models and visualization techniques could enhance the interpretability and clinical relevance of the findings. Methods such as self-attention neural networks and tensor decomposition have demonstrated effectiveness in identifying complex, non-linear patterns in neurological disorders like ADHD and Parkinson's disease[71–73]. Applying similar approaches to EEG-based tinnitus analysis could reveal more discriminative features and improve classification performance. Finally, visualizing feature distributions and model prediction boundaries would help highlight the discriminative power of the fused features, aiding clinicians in interpreting the model's decision-making process and facilitating comparisons with traditional diagnostic interpretations. Furthermore, future research should explore task-based EEG paradigms, such as auditory oddball or cognitive

workload tasks, to assess how tinnitus-related microstate dynamics vary under different cognitive and perceptual loads. Investigating task-induced changes in microstates could provide deeper insights into the functional implications of tinnitus and its impact on attentional and sensory processing.

Interpreting microstate dynamics in tinnitus presents several challenges despite their high discriminative capacity. The complexity arises from the multidimensional nature of EEG microstates, which reflect the activity of distributed neural networks rather than localized phenomena. Our systematic analysis reveals a consistent pattern of frequency-specific alterations across microstate parameters, with beta band showing the most pronounced changes related to inhibitory dysfunction. This is evidenced by increased duration of microstate A (7.8–11.2%), decreased duration of microstate B (9.0–13.8%), and elevated occurrence rates (~28–29% higher) in tinnitus patients, collectively suggesting modified cortical excitability and inhibitory control mechanisms. These beta band abnormalities align with the thalamocortical dysrhythmia model, where deafferentation promotes abnormal oscillatory activity through reduced inhibitory gating. From a clinical perspective, these microstate abnormalities may correspond to specific tinnitus symptoms; the elevated occurrence rates potentially reflect increased neural network transitions and cortical instability that could underlie tinnitus loudness or intrusiveness. Additionally, the gamma band alterations observed primarily during eyes-open conditions suggest disrupted attentional processes and heightened perceptual salience, which may explain the cognitive interference commonly reported by tinnitus patients. Future studies correlating these systematic microstate parameter changes with subjective tinnitus characteristics (loudness, distress, and quality) could establish more direct relationships between these neurophysiological markers and clinical manifestations, potentially enabling personalized therapeutic approaches targeting specific neural network configurations.

## Conclusion

This study highlights the potential of EEG microstate dynamics as neurophysiological markers for distinguishing tinnitus patients from healthy controls. By analyzing microstate parameters across multiple frequency bands, we observed consistent differences in the beta and gamma bands, which contributed to high classification performance. Notably, the deep learning model achieved 100% accuracy in the gamma band using a five-state configuration, indicating that microstate analysis effectively captures neural patterns associated with tinnitus, including altered cortical excitability and inhibitory control mechanisms. Differences between eyes-open and eyes-closed conditions further suggest that sensory context influences tinnitus-related neural activity, with gamma band changes being more prominent during visual processing and beta band alterations during sensory deprivation.

These findings provide insights into tinnitus pathophysiology and may have implications for clinical applications. The distinct microstate transition patterns in higher frequency bands align with the thalamocortical dysrhythmia model of tinnitus and may serve as potential targets for neuromodulation therapies. Additionally, transforming microstate features into 2D representations for deep learning classification offers a methodological approach that could aid in diagnosis. Future studies should explore the relationship between these microstate dynamics and subjective tinnitus symptoms, assess their stability over time, and evaluate their potential as biomarkers for treatment response. Establishing EEG microstate dynamics as reliable indicators of tinnitus-related neural alterations could contribute to the development of objective diagnostic tools and personalized intervention strategies.

## Data availability

This study used two datasets. The first dataset was collected by the authors. For access to this dataset, please contact the corresponding author. The second dataset is publicly available and can be accessed at the following link: https://data.mendeley.com/datasets/fj7sskjdt7/1.

Received: 1 November 2024; Accepted: 5 May 2025
Published online: 07 May 2025

## References

1. Pickles, J. O. *An Introduction to the Physiology of Hearing* (2008).
2. Celesia, G. G. & Hickok, G. *The Human Auditory System: Fundamental Organization and Clinical Disorders* (Elsevier, 2015).
3. Moore, B. C. *Cochlear Hearing Loss: Physiological, Psychological and Technical Issues* (Wiley, 2007).
4. McCormack, A. et al. A systematic review of the reporting of tinnitus prevalence and severity. *Hear. Res.* **337**, 70–79 (2016).
5. De Ridder, D. et al. Phantom percepts: Tinnitus and pain as persisting aversive memory networks. *Proc. Natl. Acad. Sci.* **108**(20), 8075–8080 (2011).
6. Langguth, B. A review of tinnitus symptoms beyond 'ringing in the ears': A call to action. *Curr. Med. Res. Opin.* **27**(8), 1635–1643 (2011).
7. Fetoni, A. R. et al. The evaluation of global cognitive and emotional status of older patients with chronic tinnitus. *Brain Behav.* **11**(8), e02074 (2021).
8. Martinez-Devesa, P. et al. Cognitive behavioural therapy for tinnitus. *Archivos de Prevencion de Riesgos Laborales* **16**(2), 96–97 (2013).
9. Tang, D., Li, H. & Chen, L. Advances in understanding, diagnosis, and treatment of tinnitus. In *Hearing Loss: Mechanisms, Prevention and Cure*, 109–128 (2019).
10. Shore, S. E. & Wu, C. Mechanisms of noise-induced tinnitus: Insights from cellular studies. *Neuron* **103**(1), 8–20 (2019).
11. Conlon, B. et al. Noninvasive bimodal neuromodulation for the treatment of tinnitus: Protocol for a second large-scale double-blind randomized clinical trial to optimize stimulation parameters. *JMIR Res. Protoc.* **8**(9), e13176 (2019).
12. Hébert, S. Bimodal neuromodulation of tinnitus: Finding the right wire. *Can. Audiol.* **11**(3).
13. Ibarra-Zarate, D. & Alonso-Valerdi, L. M. Acoustic therapies for tinnitus: The basis and the electroencephalographic evaluation. *Biomed. Signal Process. Control* **59**, 101900 (2020).

14. San Juan, J. et al. Tinnitus alters resting state functional connectivity (RSFC) in human auditory and non-auditory brain regions as measured by functional near-infrared spectroscopy (fNIRS). *PLoS One* **12**(6), e0179150 (2017).
15. Yang, H. et al. Diminished self-monitoring in hallucinations—Aberrant anterior insula connectivity differentiates auditory hallucinations in schizophrenia from subjective tinnitus. *Asian J. Psychiatr.* **52**, 102056 (2020).
16. Meyer-Baese, L., Watters, H. & Keilholz, S. Spatiotemporal patterns of spontaneous brain activity: A mini-review. *Neurophotonics* **9**(3), 032209–032209 (2022).
17. Makar, S. K. Etiology and pathophysiology of tinnitus: A systematic review. *Int. Tinnitus J.* **25**(1), 76–86 (2021).
18. Cai, Y. et al. Altered resting-state EEG microstate in idiopathic sudden sensorineural hearing loss patients with tinnitus. *Front. Neurosci.* **13**, 443 (2019).
19. Cai, Y. et al. Deviant dynamics of resting state electroencephalogram microstate in patients with subjective tinnitus. *Front. Behav. Neurosci.* **12**, 122 (2018).
20. Cao, W. et al. Microstate in resting state: An EEG indicator of tinnitus?. *Acta Otolaryngol.* **140**(7), 564–569 (2020).
21. Vanneste, S., To, W. T. & De Ridder, D. Tinnitus and neuropathic pain share a common neural substrate in the form of specific brain connectivity and microstate profiles. *Prog. Neuropsychopharmacol. Biol. Psychiatry* **88**, 388–400 (2019).
22. Zhang, C. et al. Study on tinnitus-related electroencephalogram microstates in patients with vestibular schwannomas. *Front. Neurosci.* **17**, 1159019 (2023).
23. Sun, Z.-R. et al. Multi-view intact space learning for tinnitus classification in resting state EEG. *Neural Process. Lett.* **49**, 611–624 (2019).
24. Zhou, S. & Su, C. Tinnitus recognition by EEG signals based on wavelet transform and deep neural networks. In *2021 International Symposium on Biomedical Engineering and Computational Biology* (2021).
25. Hong, E.-S. et al. Deep learning-based electroencephalic diagnosis of tinnitus symptom. *Front. Hum. Neurosci.* **17**, 1126938 (2023).
26. Doborjeh, M. et al. Prediction of tinnitus treatment outcomes based on EEG sensors and TFI score using deep learning. *Sensors* **23**(2), 902 (2023).
27. Liang, B. et al. Brain spontaneous fluctuations in sensorimotor regions were directly related to eyes open and eyes closed: Evidences from a machine learning approach. *Front. Hum. Neurosci.* **8**, 645 (2014).
28. Barry, R. J. et al. EEG differences between eyes-closed and eyes-open resting conditions. *Clin. Neurophysiol.* **118**(12), 2765–2773 (2007).
29. Petro, N. M. et al. Eyes-closed versus eyes-open differences in spontaneous neural dynamics during development. *Neuroimage* **258**, 119337 (2022).
30. Vecchio, F. et al. Entropy as measure of brain networks' complexity in eyes open and closed conditions. *Symmetry* **13**(11), 2178 (2021).
31. Gruters, K. G. et al. The eardrums move when the eyes move: A multisensory effect on the mechanics of hearing. *Proc. Natl. Acad. Sci.* **115**(6), E1309–E1318 (2018).
32. Alonso-Valerdi, L. M., González-Salazar, J. I. & Ibarra-Zarate, D. I. Neuropsychological monitoring of current acoustic therapies as alternative treatment of chronic tinnitus. *Am. J. Otolaryngol.* **42**(6), 103109 (2021).
33. Widmann, A., Schröger, E. & Maess, B. Digital filter design for electrophysiological data—A practical approach. *J. Neurosci. Methods* **250**, 34–46 (2015).
34. Delorme, A. & Makeig, S. EEGLAB: An open source toolbox for analysis of single-trial EEG dynamics including independent component analysis. *J. Neurosci. Methods* **134**(1), 9–21 (2004).
35. Klimesch, W. EEG alpha and theta oscillations reflect cognitive and memory performance: A review and analysis. *Brain Res. Rev.* **29**(2–3), 169–195 (1999).
36. Michel, C. M. & Koenig, T. EEG microstates as a tool for studying the temporal dynamics of whole-brain neuronal networks: A review. *Neuroimage* **180**, 577–593 (2018).
37. Khanna, A. et al. Microstates in resting-state EEG: Current status and future directions. *Neurosci. Biobehav. Rev.* **49**, 105–113 (2015).
38. Zebhauser, P. T., Hohn, V. D. & Ploner, M. Resting state EEG and MEG as biomarkers of chronic pain: A systematic review. *Pain* (2022).
39. Lehmann, D. & Skrandies, W. Reference-free identification of components of checkerboard-evoked multichannel potential fields. *Electroencephalogr. Clin. Neurophysiol.* **48**(6), 609–621 (1980).
40. Pascual-Marqui, R. D., Michel, C. M. & Lehmann, D. Segmentation of brain electrical activity into microstates: Model estimation and validation. *IEEE Trans. Biomed. Eng.* **42**(7), 658–665 (1995).
41. Bagherzadeh, S., Shahabi, M. S. & Shalbaf, A. Detection of schizophrenia using hybrid of deep learning and brain effective connectivity image from electroencephalogram signal. *Comput. Biol. Med.* **146**, 105570 (2022).
42. Bagherzadeh, S. et al. Emotion recognition using effective connectivity and pre-trained convolutional neural networks in EEG signals. *Cogn. Neurodyn.* **16**(5), 1087–1106 (2022).
43. Nair, V. & Hinton, G. E. Rectified linear units improve restricted boltzmann machines. In *Proceedings of the 27th International Conference on Machine Learning (ICML-10)* (2010).
44. Srivastava, N. et al. Dropout: A simple way to prevent neural networks from overfitting. *J. Mach. Learn. Res.* **15**(1), 1929–1958 (2014).
45. Ioffe, S. *Batch normalization: Accelerating deep network training by reducing internal covariate shift*. arXiv preprint arXiv:1502.03167 (2015).
46. Ke, H. et al. Improving brain E-health services via high-performance EEG classification with grouping Bayesian optimization. *IEEE Trans. Serv. Comput.* **13**(4), 696–708 (2019).
47. Simonyan, K. & Zisserman, A. *Very deep convolutional networks for large-scale image recognition*. arXiv preprint arXiv:1409.1556 (2014).
48. He, K., et al. Deep residual learning for image recognition. In *Proceedings of the IEEE Conference on Computer Vision and Pattern Recognition* (2016).
49. Chollet, F. Xception: Deep learning with depthwise separable convolutions. In *Proceedings of the IEEE Conference on Computer Vision and Pattern Recognition* (2017).
50. Breiman, L. *Classification and Regression Trees* (Routledge, 2017).
51. Breiman, L. Random forests. *Mach. Learn.* **45**, 5–32 (2001).
52. Cortes, C. & Vapnik, V. Support-vector networks. *Mach. Learn.* **20**, 273–297 (1995).
53. Zhu, W., Zeng, N. & Wang, N. Sensitivity, specificity, accuracy, associated confidence interval and ROC analysis with practical SAS implementations. In *NESUG Proceedings: Health Care and Life Sciences, Baltimore*, vol. 19, p. 67 (2010).
54. Wang, C.-D. et al. Cross-subject tinnitus diagnosis based on multi-band EEG contrastive representation learning. *IEEE J. Biomed. Health Inform.* **27**(7), 3187–3197 (2023).
55. Jianbiao, M. et al. EEG signal classification of tinnitus based on SVM and sample entropy. *Comput. Methods Biomech. Biomed. Eng.* **26**(5), 580–594 (2023).
56. Wang, Y. et al. Objective neurophysiological indices for the assessment of chronic tinnitus based on EEG microstate parameters. In *IEEE Transactions on Neural Systems and Rehabilitation Engineering* (2024).
57. Zhu, M. & Gong, Q. EEG spectral and microstate analysis originating residual inhibition of tinnitus induced by tailor-made notched music training. *Front. Neurosci.* **17**, 1254423 (2023).

58. Ke, H. et al. Cloud-aided online EEG classification system for brain healthcare: A case study of depression evaluation with a lightweight CNN. *Softw. Pract. Exper.* **50**(5), 596–610 (2020).
59. Vanneste, S., Song, J.-J. & De Ridder, D. Thalamocortical dysrhythmia detected by machine learning. *Nat. Commun.* **9**(1), 1103 (2018).
60. De Ridder, D. et al. Thalamocortical dysrhythmia: A theoretical update in tinnitus. *Front. Neurol.* **6**, 124 (2015).
61. Czornik, M. et al. Psychophysiological treatment of chronic tinnitus: A review. *Clin. Psychol. Psychother.* **29**(4), 1236–1253 (2022).
62. Sedley, W. et al. An integrative tinnitus model based on sensory precision. *Trends Neurosci.* **39**(12), 799–812 (2016).
63. Weisz, N. et al. The neural code of auditory phantom perception. *J. Neurosci.* **27**(6), 1479–1484 (2007).
64. van Der Loo, E. et al. Tinnitus intensity dependent gamma oscillations of the contralateral auditory cortex. *PLoS One* **4**(10), e7396 (2009).
65. Sedley, W. et al. Exposing pathological sensory predictions in tinnitus using auditory intensity deviant evoked responses. *J. Neurosci.* **39**(50), 10096–10103 (2019).
66. Almasabi, F. Deep brain stimulation in tinnitus: Insights from the pathophysiology and mechanism of action (2022).
67. De Ridder, D. et al. An integrative model of auditory phantom perception: Tinnitus as a unified percept of interacting separable subnetworks. *Neurosci. Biobehav. Rev.* **44**, 16–32 (2014).
68. Shalbaf, A., Bagherzadeh, S. & Maghsoudi, A. Transfer learning with deep convolutional neural network for automated detection of schizophrenia from EEG signals. *Phys. Eng. Sci. Med.* **43**, 1229–1239 (2020).
69. Chaddad, A. et al. Electroencephalography signal processing: A comprehensive review and analysis of methods and techniques. *Sensors* **23**(14), 6434 (2023).
70. Chen, Y. C. et al. Tinnitus distress is linked to enhanced resting-state functional connectivity from the limbic system to the auditory cortex. *Hum. Brain Mapp.* **38**(5), 2384–2397 (2017).
71. Ke, H. et al. Unsupervised deep frequency-channel attention factorization to non-linear feature extraction: A case study of identification and functional connectivity interpretation of Parkinson's disease. *Expert Syst. Appl.* **243**, 122853 (2024).
72. Ke, H. et al. Deep factor learning for accurate brain neuroimaging data analysis on discrimination for structural MRI and functional MRI. In *IEEE/ACM Transactions on Computational Biology and Bioinformatics* (2023).
73. Ke, H. et al. ADHD identification and its interpretation of functional connectivity using deep self-attention factorization. *Knowl.-Based Syst.* **250**, 109082 (2022).



## Acknowledgements
We acknowledge Reza Ahmadi Lashaki for his initial contribution to data processing; however, his role was not sufficient to justify continued authorship. The authors would like to acknowledge the Iranian National Brain Mapping Laboratory (NBML), Tehran, Iran, for providing data acquisition (analysis) service for this research work.


## Author contributions
Z.R. conceptualized the study, conducted EEG data analysis, and implemented the model. A.S. contributed to statistical modeling, data interpretation, and validation. F.S. developed algorithms and engineered features. A.R. implemented the software and optimized the deep learning model. H.N. evaluated clinical data and provided medical expertise. O.B. handled EEG preprocessing, feature extraction, and methodology refinement. A.G. assisted with data analysis, performed statistical evaluations, and contributed to the interpretation of the results. All authors contributed to the interpretation of results, refined the discussion section, and approved the final manuscript.

## Declarations

## Competing interests
The authors declare no competing interests.

## Ethics declarations
All experimental protocols were approved by the Ethics Committee of Tabriz University of Medical Sciences, Tabriz, Iran, in accordance with the principles of the Declaration of Helsinki.

## Additional information
**Correspondence** and requests for materials should be addressed to H.N.

**Reprints and permissions information** is available at www.nature.com/reprints.

**Publisher's Note** Springer Nature remains neutral with regard to jurisdictional claims in published maps and institutional affiliations.
**Publisher's note** Springer Nature remains neutral with regard to jurisdictional claims in published maps and institutional affiliations.

**Open Access** This article is licensed under a Creative Commons Attribution-NonCommercial-NoDerivatives 4.0 International License, which permits any non-commercial use, sharing, distribution and reproduction in any medium or format, as long as you give appropriate credit to the original author(s) and the source, provide a link to the Creative Commons licence, and indicate if you modified the licensed material. You do not have permission under this licence to share adapted material derived from this article or parts of it. The images or other third party material in this article are included in the article's Creative Commons licence, unless indicated otherwise in a credit line to the material. If material is not included in the article's Creative Commons licence and your intended use is not permitted by statutory regulation or exceeds the permitted use, you will need to obtain permission directly from the copyright holder. To view a copy of this licence, visit http://creativecommons.org/licenses/by-nc-nd/4.0/.

© The Author(s) 2025